Holocene Relative Sea-Level Changes along the Caribbean and Pacific Coasts of Northwestern South America

Juan F. Paniagua-Arroyave[a,b,c], Giorgio Spada[d], Daniele Melini[e], José F. Duque-Trujillo[f]

[a] Area of Natural Systems and Sustainability, School of Applied Sciences and Engineering, EAFIT University, Colombia

[b] Department of Physical Geography, Faculty of Geosciences, Utrecht University, The Netherlands

[c] INSTAAR, University of Colorado Boulder, United States of America

[d] Dipartimento di Fisica e Astronomia (DIFA), Settore Geofisica, Alma Mater Studiorum Università di Bologna, Italia

[e] Istituto Nazionale di Geofisica e Vulcanologia, Roma, Italia

[f] Area of Territories and Cities, School of Applied Sciences and Engineering, EAFIT University, Colombia

Corresponding author address: Escuela de Ciencias Aplicadas e Ingeniería, Universidad EAFIT, Carrera 49 # 7 Sur – 50, Medellín, Antioquia 050022, Colombia.

E-mail address: jpaniag2@eafit.edu.co, juan.paniaguaarroyave@colorado.edu (Juan F. Paniagua-Arroyave)

Abstract

Predicting coastal change depends upon our knowledge of postglacial relative sea-level variability, partly controlled by glacio-isostatic responses to ice-sheet melting. Here, we reconstruct the postglacial relative sea-level change along the Caribbean and Pacific coasts of Northwestern South America by numerically solving the Sea-Level Equation with two scenarios of mantle viscosity: global standard average and high viscosity. Our results with the standard model (applicable to the Pacific coast) agree with earlier studies by indicating a mid-Northgrippian highstand of meters. The high viscosity simulation (relevant to the Caribbean coast) shows that the transition from far- to intermediate-field influence of the Laurentide ice sheet occurs between Manzanillo del Mar and the Gulf of Morrosquillo. South of this location, the Colombian Caribbean coast has exhibited a stillstand with a nearly constant Holocene relative sea level. By analyzing our simulations considering sea-level indicators, we argue that tectonics is more prominent than previously assumed, especially along the Caribbean coast. This influence prevents a simplified view of regional relative sea-level change on the Northwestern South American coast.

Keywords: glacial isostatic adjustment; GIA; equatorial ocean siphoning; continental levering; mud diapirism; Caribbean coast; Pacific coast; Colombia; paleo sea-level markers; glacial isostatic adjustment model; mantle viscosity model.

1. Introduction

Predicting coastal change depends upon deciphering postglacial relative sea-level (SL) variability and its influence on modern morphology (FitzGerald et al., 2008; Passeri et al., 2015). Postglacial relative sea-level (RSL) changes control modern coastal environments as they dictate nearshore sediment accommodation and supply (Everts, 1987; Törnqvist et al., 2020). Thus, refining our knowledge of postglacial RSL within a morphodynamic framework allows us to quantify coastal response in an increasingly human-influenced world (Kopp et al., 2015; Nerem et al., 2018; Nicholls and Cazenave, 2010; Nienhuis and van de Wal, 2021).

Here, we compare postglacial RSL change simulations with available SL indicators for the Caribbean and Pacific coasts of Northwestern (NW) South America to decipher the spatial-temporal variability of Holocene RSL. Understanding such variability would require unraveling the Glacial Isostatic Adjustment (GIA) response, which is critical for understanding the RSL drivers. We focus on an outstanding question: *What GIA processes are responsible for RSL change, intermediate- or far-field?*

Considering the coastal evolution of NW South America, tectonics creates a complex deformation that prevents a simplified view of continental vertical change influencing RSL (Garrett et al., 2020). In addition, exploring postglacial RSL change informs us about modern coastal morphodynamics. Any RSL framework would imply either transgressive (intermediate-field) or regressive (far-field) conditions during the Holocene with implications for contemporary coastal change (Nienhuis et al., 2023; Shadrick et al., 2022).

Our work is organized as follows. Section 2 (Background) includes information on postglacial relative SL changes, the geology of coastal Colombia, postglacial RSL changes along NW South America, and GIA modeling. Section 3 (Methods) outlines details of our RSL change simulations with SELEN^4 and the compilation of SL indicators. Section 4 (Results) presents our results in three subsections: modeled postglacial RSL change, modeled Holocene RSL change, and compiled SL indicators (see the compilation in the Supplemental Information at http://dx.doi.org/10.17632/7nhpbhvfnz.2). Section 5 (Discussion) discusses ocean versus ice loadings within GIA modeling, three-dimensional

Earth structure along NW South America, the role of tectonics in RSL change, and sediment isostasy. We provide our Conclusions in section 6.

2. Background

2.1. Postglacial RSL Change

Coastal change in the 21st Century will be multifaceted, depending on marine and continental processes that modify the coastal terrain (Anfuso et al., 2021; Kennedy et al., 2020; Nienhuis et al., 2020 and others). In turn, the extent of coastal processes depends on RSL, which is determined by climatic, oceanographic, and solid Earth processes, including GIA, that control the relative position of the continental and ocean surface levels (Gregory et al., 2019; Milne et al., 2009; Pirazzoli, 1996, pp. 5).

During the Holocene (last 11.7 ka, Walker et al., 2018), GIA controlling RSL depended on the location on Earth (Kopp et al., 2015; Lambeck et al., 2011). Locally, ocean and continental surfaces varied because ice melting redistributed ocean water, the Earth's rotation changed, and the lithosphere was deformed by water, sediment, and ice loads (Rovere et al., 2016). Therefore, ice sheet melting produced GIA responses that depended on local conditions, i.e., inner Earth structure and distance from the ice sheets (Whitehouse, 2018).

In the far field (away from the immediate influence of ice-sheet forebulge collapse), hydro-isostatic balances dominated after the ice melted and gravitational effects ceased (Clark et al., 1978). This process created mid-Holocene highstands that implied RSL fall and marine regression during the Late Holocene. Evidence of this regression (e.g., beach ridges, strandplains, fluvial-marine terraces) is ubiquitous in the far field along tectonically inactive regions (Cooper et al., 2018; Hein et al., 2014; Isla, 1989). This regression contrasts with the transgression caused by a gradual inundation along coasts in the intermediate field, i.e., controlled by the collapse of the ice sheet forebulge that lowered the solid Earth and rose RSL. Such postglacial history implies coastline retreat with submerged evidence of Holocene transgression (Mitrovica and Peltier, 1991).

When analyzing RSL changes along NW South American coasts, as it is (geologically) separated in the Pacific and Caribbean by the Panama Isthmus, we find a dichotomy in whether intermediate- or far-field GIA processes have dominated during the Holocene. Therefore, we resort to separating the Caribbean from the Pacific coasts in our analysis. Arguably, the low-latitude location makes far-field effects dominant. Also, the Caribbean coast (especially the northern region) will likely be at the limit of intermediate-field influence from the Laurentide ice sheet collapse (Khan et al., 2015). We, therefore, explore the dichotomy between intermediate- or far-field dominance, with the hypothesis of GIA varying latitudinally along the NW South American coast. If intermediate-field effects dominate, RSL changes will exhibit a continuous rise (e.g., Louisiana, USA; Khan et al., 2015, Fig. 3F). In contrast, if far-field effects dominate, RSL changes would exhibit a mid-Holocene highstand, i.e., an RSL higher than the present, typically at –6 ka (e.g., Rio Grande do Norte, Brazil; Khan et al., 2015, Fig. 3I). See also Yokoyama and Purcell (2021, their Fig. 8) for additional schematics.

2.2. Geology of NW South America and Coastal Colombia

Northwestern South America exhibits a complex geological setting that frames coastal evolution and postglacial RSL changes (Figure 1). Here, we focus on the features influencing crustal motions controlling postglacial RSL changes. For in-depth accounts of the geology and tectonics of NW South America, we suggest seminal works by Nygren (1950), Duque-Caro (1990a, 1990b), Vernette et al. (1992), Kellogg and Vega (1995), Colmenares and Zoback (2003), and IGAC and INGEOMINAS (2006), as well as more recent accounts by Cediel and Shaw (2019), Montes et al. (2019), Bustamante et al. (2023, 2016), Restrepo et al. (2023, 2021), and references therein.

The tectonic framework of NW South America is given by the junction of three tectonic plates, two oceanic (Nazca and Caribbean) and one continental (South American), which creates two subduction zones. Each subduction zone corresponds to either the Caribbean or the Pacific coast of Colombia and decisively determines the coastal geology of each coast (Correa and Pereira, 2019). Both coasts can be considered collisional (Inman and Nordstrom, 1971). However, their coastal environments differ, ranging from spits, lagoons, mangrove swamps, and beach and dune complexes to plunging cliffs, cliffs-shore platforms, and pocket beaches (Correa and Morton, 2010a, 2010b).

Geology frames six coastal fringes along the Caribbean (Figure 2) (Correa and Morton, 2010a; Correa and Pereira, 2019). The Gulf of Urabá’s western margin exhibits an oceanic magmatic arc that creates plunging cliffs and pocket beaches, contrasting with intertidal Quaternary deposits (beaches-dunes, lagoons) to the south and eastern margins (Correa et al., 2016). North of the Gulf of Urabá, the Quaternary deposits switch to fluvial-marine terraces that emerged during the last ~5 ka by tectonics and (apparently) hydro-isostasy (Correa and Paniagua-Arroyave, 2016). These terraces form out of sediments from a Cenozoic accretionary prism called the Sinu-San Jacinto Deformed Belt, spanning the coastal fringe to the Magdalena river delta, except for the Gulf of Morrosquillo, which forms in beach-dune and lagoon deposits. North of the Magdalena River Delta, there are plunging cliffs associated with the Cretaceous/Jurassic metamorphic rocks of the Santa Marta Massif. Finally, we find Quaternary deposits (beach, dunes, and lagoons with aeolian deposits) from the Sierra Nevada of Santa Marta to the Guajira Peninsula (Correa and Pereira, 2019).

Along the Pacific coast, the subduction of the Nazca underneath the South American plate is relatively steep, which produces a narrow continental shelf and accumulation zones (Figure 3). The coastal zone is flanked by an oceanic plateau fragment (related to the Cali-Patia fault system) to the East and the Garrapatas fault to the North (González et al., 2014; Montes et al., 2019). The steep subduction has produced folding and faulting systems along regional lineaments. As a result, there are four major coastal blocks and basins: the Baudo Mountain Range, the Atrato Basin, the San Juan Basin, and the Tumaco Basin (IGAC and INGEOMINAS, 2006). The coastal morphology is characterized by Quaternary deposits related to the Patia, San Juan, Mira, and other smaller deltas that deposit in the accommodation created by geological structures (Correa, 1996; Correa and Morton, 2010b). The coastal environments are depositional to the south, primarily wave-tidally-dominated deltas with meso-tidal barrier islands, beaches, and mangrove swamps. To the north, an oceanic plateau fragment (the Baudó Mountain Range) is found at the ocean-continent intersection, creating plunging cliffs and related erosional environments (Correa and Pereira, 2019).

In NW South America, horizontal crustal deformation has been measured with GPS technology, obtaining a NE (060°) motion of the Northern Andean Block at 8.6 mm/year, an eastward collision of the Panama arc at 15-18 mm/year, and a Caribbean subduction at 13 mm/year. Due to significant uncertainties, vertical motions have not yet been published (Mora-Páez et al., 2019). In addition to faulting-related tectonics, vertical motions contributing to RSL change also depend on mud diapirism along both coasts (Carvajal, 2016; Martínez and López Ramos, 2010) and co-seismic motions linked to major earthquakes, with at least seven events of Mw>7.0 since 1906 along the Pacific coast (Figure 3) (González and Correa, 2001).

Along both coasts, especially the Caribbean, crustal kinematics get exacerbated by mud diapirism upwarping the littoral fringe and continental shelf (Carvajal, 2016; Naranjo-Vesga et al., 2020). Mud diapirism manifests on- and offshore by dome-type features, mud, and gas emissions (Vivas-Narváez, 2019). For example, along Minuto de Dios, north of Arboletes town (Figure 2), alongshore cliff-top elevations evidence an inclination towards the central mud volcano (Paniagua-Arroyave et al., 2018).

With this complex geological framework in mind, we now explore the evidence of RSL changes along the NW South American coast.

2.3. Evidence of Holocene RSL Changes along NW South America

Local studies have documented SL indicators in emerged terraces (Martínez et al., 2010; Page, 1982), sequences of organic deposits in coastal lagoons (González, 2017), drowned (Page and James, 1981), and raised beaches (González et al., 2014). These studies highlight the tectonic motions as the most prominent process and main unknown. Despite the effort to document such SL indicators in remote locations, these records are difficult to analyze regarding postglacial RSL change, given the knowledge gap in tectonics and local GIA.

Considering the local GIA in the Caribbean, recent studies suggest that intermediate-field processes control the Holocene RSL change (González, 2017; Khan et al., 2017). These analyses used a set of available SL indicators and state-of-the-art statistical models to elucidate the RSL variability. They argue that RSL has been rising during the past millennia due to the influence of the Laurentide forebulge collapse that induces crustal lowering with a constant ocean level. However, we hypothesize that the Caribbean coast of NW South America is within the limit of influence from such intermediate effects. We support our argument by highlighting several dubious assumptions in other authors' work. The inconsistencies include: (1) assuming the central Caribbean coast does not exhibit tectonic deformation (González, 2017) and (2) including SL indicators from an island several hundreds of kilometers away from the Caribbean coast of NW South America (Khan et al., 2017).

We argue against the dominance of intermediate-field effects along the Caribbean, in line with recent evidence on crustal deformation. There is an ongoing discussion in favor of a “crustal block” model for the Caribbean coast of NW South America (Gómez-Álvarez, 2022), aligned with seminal contributions for the Pacific (Correa, 1996). In that vein, a recent study combined in situ instrumentation and remote sensing to propose that compressive tectonics controls RSL rise near Cartagena City by crustal subsidence (Restrepo-Ángel et al., 2021). In other words, tectonics can also lower the crust (and rise SL) along the Caribbean and Pacific coasts of NW South America. Therefore, SL indicators from coastal lagoons (e.g., Urrego et al., 2013) ought to be the submerged counterparts of SL indicators from emerged morphology, such as raised corals or marine terraces (e.g., Martínez et al., 2010).

The crustal block model can also explain RSL change in the Pacific. Seminal works demonstrated the interdependence of hydrodynamics, sediment supply/accommodation, and local crustal structures, with coastal morphology manifesting in active and inactive cliffs, bays, and deltas (Correa, 1996). Furthermore, co-seismic motions add to the crustal block kinematics, such that Holocene RSL indicators above the present mean SL can appear even without postglacial GIA far-field effects (González et al., 2014; Page and James, 1981). Mud diapirism along the Pacific coast should also control RSL, although the evidence is limited (Martínez and López Ramos, 2010).

We highlight two issues with the current knowledge of postglacial RSL along the NW South American coasts. First, the results that support a dominance of intermediate-field effects depend on RSL indicators biased toward coastal lagoons irrespective of local tectonics. Second, tectonics creates a complex terrain deformation that prevents a simplified view of continental vertical change compared to local SL indicators, i.e., inferring regional RSL changes from discrete locations. Therefore, we attempt to resolve these issues by simulating postglacial RSL changes with the best-suited Earth rheology models and analyze our simulations using the available SL indicators.

2.4. Modeling Postglacial RSL in NW South America

Regional studies calibrated GIA models with local SL indicators for portions of the South American and Caribbean passive margins to elucidate the postglacial meltwater contribution to RSL changes (Milne et al., 2005; Milne and Peros, 2013). These studies also explained contributions from the ocean, ice, and rotational components on Holocene RSL change, with far-field effects influencing all South American coastlines and intermediate-field effects dominating the Caribbean. A critical part of these studies was finding the Earth rheology that explained the RSL change observations.

Here, we analyze the spatial variability in Holocene RSL changes along NW South America by exploring Earth rheology models in numerical simulations of postglacial RSL. We then compare the simulations with SL indicators to analyze the influence of crustal kinematics and solid Earth rheology. We emulate a recent contribution that examined Holocene RSL in the tectonically active Chilean region by reassessing SL indicators and contrasting them to GIA modeling (Garrett et al., 2020). We highlight how subduction styles and crustal deformation decisively control postglacial RSL change along the NW South American coasts.

3. Methods

3.1. GIA Modeling of Postglacial RSL Change

We modeled postglacial RSL changes along the NW South American coast (Figure 4, Figure 5, and Table 1) by solving the Sea Level Equation (SLE). The SLE, first introduced by Farrell and Clark (1976), provides a self-consistent quantitative description of the physical interactions between the cryosphere, oceans, and solid Earth in response to the melting of ice sheets. We obtained numerical solutions of the SLE with the open-source SELEN^4 code (Spada and Melini, 2019), which is based on the pseudospectral method and considers the horizontal migration of shorelines (Peltier, 2004) and rotational feedback (Milne and Mitrovica, 1998). The numerical solution has been obtained on a global icosahedron grid (Tegmark, 1996) with resolution R=44, corresponding to a spatial resolution of about 90 km on the Earth's surface.

In our solutions of the SLE, the spatial-temporal evolution of ice sheets is assumed to follow the ICE-6G_C GIA model of Peltier et al. (2015), which has been converted to a piecewise constant time history, as required by SELEN^4, with a constant time step of 500 years from –26 ka to 0 ka (present). The Earth's internal structure is assumed to be spherically symmetric, with incompressible, linear (Maxwell type) mantle rheology, elastic lithosphere, and inviscid fluid core. Consistently with the ICE-6G_C GIA model, the radial structure is assumed to follow the VM5 rheological profile (Peltier and Drummond, 2008).

To represent the different subduction styles along the Caribbean and Pacific coasts, we explored two different mantle viscosity scenarios: a standard viscosity (that accounts for global data, VM5i from Spada and Melini, 2019) (Table 2) and a high viscosity model according to previous studies that we called "VM5h" (Milne et al., 2005; Milne and Peros, 2013) (Table 3). We applied the same ice history ICE-6G_C from Peltier et al. (2015) with both models.

Note that only our standard (VM5i) model reconciles simulations with global RSL data for a given ice thickness history (model ICE-6G_C of Peltier et al., 2015), as applied elsewhere (see Spada and Melini, 2022 and others). However, changing the viscosity profile without varying the ice thickness history creates a mismatch with local RSL observations. Our high-viscosity model does not intend to reconcile simulations with global SL indicators. Instead, we want to analyze the GIA simulations with a plausible Earth rheology to compare to the available RSL indicators for the NW South American coasts.

3.2. NW South American RSL indicators

We compiled SL indicators available for the NW South American coasts, considering, whenever possible, their "fundamental characteristic attributes" as proposed in the literature: geographic location, age of formation, elevation to contemporary tidal datum, and relationship to RSL (Khan et al., 2019). Sea-level indicators comprise coastal sediments (for correlations with marine-terrestrial transitions within the stratigraphic record) and geomorphic evidence (corals, terraces-cliffs, beach ridges), with corresponding dating and laboratory techniques to quantify ages and characterize environments. The compiled SL indicators fall into geomorphological (emerged terraces), coastal sediments, and coral reefs categories (Shennan et al., 2015).

We included 62 indicators (54 for the Caribbean and 8 for the Pacific) comprising coastal lagoon sediments, beach sediments, mollusk shells, and corals, with ages given by radiocarbon and optically stimulated luminescence dating. Given the heterogeneous and sometimes lacking details about their methodologies (including geodetic elevations), we included time and vertical location uncertainties according to the literature (Engelhart et al., 2011; Engelhart and Horton, 2012; Khan et al., 2017).

To use a standard temporal frame, we quantified the calibrated years for the 59 radiocarbon dates available using the MatCal v3.1 routine in MATLAB® (Lougheed and Obrochta, 2016), with Marine20 and IntCal20 calibration curves, $\Delta R = -19 \pm 23$ ^{14}C yr (Caribbean reservoir effect, Martínez et al., 2010) and $R(t) = -198 \pm 163$ ^{14}C yr (Pacific, Reimer and Reimer, 2001). We referenced all dates to 1950 AD as "present," including beach sediments (3 dates) at Bajo Baudó (Pacific site 5) dated by optically stimulated luminescence from Gonzalez et al. (2014).

In terms of radiocarbon ages and simulated RSL changes, we have a total of 12 dates related to Minuto de Dios (Caribbean site 2), 5 to the Gulf of Morrosquillo (Caribbean site 3), 7 to Manzanillo del Mar (Caribbean site 4), 6 to the Magdalena River delta

(Caribbean site 5), 4 to the Ranchería River delta (Caribbean site 6), 2 to Utría Cove (Pacific site 6), and 5 to Solano Bay (Pacific site 7).

4. Results

4.1. Modeled Postglacial RSL Changes

Figure 6 and Figure 7 show the modeled RSL changes for NW South American (Caribbean and Pacific) coasts from the standard (VM5i) and high (VM5h) viscosity scenarios. We include postglacial (Figure 6A and Figure 7A) and Holocene changes (Figure 6B and Figure 7B).

At millennial timescales, variations in time and space are insignificant on both coasts. Both viscosity models predicted RSL ~100 m below the present level at ~–26 ka. Relative SL increased from ~–100 m to ~–80 m between –26 and –14 ka, then increased rapidly to ~–60 m between –14 and –13 ka, linked to the Melt Water Pulse 1A (Liu et al., 2015; Liu and Milliman, 2004). Then, both models predict an increase in RSL until –6 ka and a relatively constant RSL from –6 ka to the present.

The difference in Holocene RSL change between models is evident from the mid-Northgrippian (–6 ka) to the present. The standard model predicts a highstand and RSL fall, whereas the high viscosity model predicts either an RSL rise or a stillstand. Overall, the RSL changes for the standard model represent the response to hydro-isostatic effects along continental shelves in the far field of ice sheets (Clark et al., 1978). In contrast, the high-viscosity model results include far- and intermediate-field effects (Engelhart et al., 2009).

4.2. Modeled Holocene RSL Changes

Figure 8 and Figure 9 show the mid and Late Holocene RSL changes along the NW South American coast. For the Caribbean (Figure 8A), the standard model predicts an RSL highstand of ~2 m around –6 ka at the southern locations (e.g., Minuto de Dios, site 2, and Gulf of Morrosquillo, site 3), similar to the Zone VI of continental shorelines from Clark et al. (1978). This peak is in the order of centimeters at the northern locations (e.g., Caribbean site 7, Guajira Peninsula, and site 5, Magdalena River Delta). The highstand also shifts in time, from ~–6 ka in the south to ~–3 ka in the north. These results are consistent with extensive morphological observations that suggest coastal change depends on a regional RSL change related to postglacial hydro-isostatic effects (Correa, 1990; Correa et al., 2016, 2007, 2005; Correa and Morton, 2010a; Correa and Vernette, 2004). This scenario implies a late Holocene RSL fall of ~2 m in 6 ka, or –0.33 mm/a, and marine regression at the southern sites. This framework would result in Holocene SL indicators above the present mean SL, such as raised beaches and abandoned cliffs (Dougherty et al., 2019).

The high viscosity simulations for the Caribbean (Figure 8B) suggest that during the Meghalayan age (–4.2 ka to present), RSL changes have depended on intermediate-field effects related to the Laurentide proglacial forebulge collapse, as in Zone IV of marine submergence from Clark et al. (1978). This scenario concurs with recent studies, where RSL indicators obtained at (presumably) tectonically stable sites suggest a gradual marine transgression during the last 4 ka (González, 2017; Vélez et al., 2014). Like the standard model, simulations predicted higher values for southern locations (e.g., Gulf of Morrosquillo, Caribbean site 3), in contrast to northern areas with RSL curves ~0.5 m below the southern zones (e.g., Guajira Peninsula, Caribbean site 7). These curves suggest a Late Holocene RSL stillstand at the northern sites and a marine transgression of ~1 m in the last ~2 ka (+0.5 mm/a) at the southern sites.

Holocene RSL curves for the Pacific coast show spatially homogeneous Mid-Holocene highstands for both models (Figure 9). For the standard model (more representative of the Pacific subduction), we predicted a ~2 m highstand (height variability of ~0.5 m among sites), with an RSL fall of ~2 m in 6 ka (–0.33 mm/a) during the late Holocene. On the other hand, we predicted a mid-Holocene highstand 0.50 m for the high viscosity model (height variability of ~0.5 m among sites), with a variable RSL fall: –0.5 m in 6 ka (–0.083 mm/a) at the Naya River mouth (site 3) compared to –0.10 m in 2 ka (–0.05 mm/a) at the Patia River delta (site 2). We did not predict an RSL rise during the late Holocene for the high-viscosity scenario, in contrast to the results for the Caribbean.

4.3. Compiled Sea Level Indicators

We now compare our GIA simulations with the compiled SL indicators. On the Caribbean coast, SL indicators from marine fossils are typically above modeled RSL curves for both mantle models (Figure 10B-D). These indicators correspond to emerged marine terraces or corals from the Meghalayan age (–4.2 ka to present) (Correa and Paniagua-Arroyave, 2016; Page, 1982) that result from the combination of postglacial hydro-isostasy, tectonics (Martínez et al., 2010; Restrepo-Ángel et al., 2021), and mud diapirism (Naranjo-Vesga et al., 2020).

Conversely, Caribbean indicators from coastal lagoons are below the RSL predictions (Figure 10E-F). For example, near the Gulf of Morrosquillo (Caribbean site 3 in Figure 4A), González (2017) reported RSL values of –1.6 m at –4.3 ka and –0.4 m at –7.3 ka (Figure 10C) that follow the marine transgression predicted by our high viscosity model at the northern Caribbean sites (Figure 8B).

On the Pacific coast, previous studies reported ~2 m raised beaches at Terco and Termales near the Corrientes Cape (Pacific site 5) (González et al., 2014) (Figure 11B). The active tectonics, as well as GIA, can explain the raised beaches. For the dates –3 ka found by colleagues, our high mantle viscosity model predicts raised beaches ~1.0 m above the current mean SL.

Finally, the SL indicators of coastal lagoons in the Pacific are below our predictions (Figure 11C-D). Previous studies interpreted submerged SL indicators at Solano Bay as representative of co-seismic subsidence (Page and James, 1981), in contrast to the hydro-isostatic mechanisms. We argue that emergence or subsidence occurs on both coasts: the coastal fringe can either emerge or subside, with correspondent RSL fall or rise due to faulting-folding and block stacking: the “crustal block” model.

Our comparison of GIA simulations and SL indicators provides two insights. First, tectonics seems more prominent than expected, as RSL can also fall by crust subsidence. Second, GIA simulations suggest the Pacific and Caribbean differ in which GIA process dominates, with the transition from intermediate to far-field effects occurring on the Caribbean coast.

5. Discussion

This work compares simulations of postglacial RSL changes with available SL indicators along the NW South American coasts to analyze its spatial variability and drivers. We applied two scenarios of mantle rheology (standard and high viscosities) and compared the results to published SL indicators. Sea-level indicators are above or below our predictions according to compressive tectonics that produced emergence or subsidence. We now discuss our GIA simulations regarding its mechanisms (intermediate- and far-field processes). Then, we discuss how tectonics influences RSL change through GIA response (solid Earth rheology and subduction styles) and solid Earth deformation (crustal block model).

5.1. Modeling Postglacial RSL: Ocean versus Ice Loadings

We consider the main uncertainties associated with GIA RSL modeling: Earth's structure and modeling approach (Melini and Spada, 2019). From seminal works, it is well known that the postglacial ice sheet waning influenced low-latitude coastlines by water flux from equatorial regions to zones exhibiting forebulge collapse (Mitrovica and Milne, 2002; Mitrovica and Peltier, 1991). This collapse induced a Holocene RSL fall because the water flux from far- to intermediate-field regions drove a long-term SL fall after the instantaneous rise because of ice sheet melting (i.e., "ocean siphoning"). In addition, the added ocean water on continental shelves "tilted" the continents towards the sea and emerged the coastal fringes (i.e., "continental margin levering") (Clark et al., 1978). Therefore, postglacial GIA RSL models usually differentiate two loadings: "ice" from the forebulge collapse and "ocean" from continental shelf hydroisostasy.

Regional simulations with a standard solid Earth model suggest that the ocean loading happens along South America's coasts, with mid-Northgrippian (–7 ka) ~2 m high stands along the southern Caribbean and northern Pacific coasts of NW South America (Milne et al., 2005). Spatially, the ocean component of these simulations includes a gradient in RSL change perpendicular to the general coastline orientation, with a zero RSL change coinciding with the coastline near the Magdalena River delta. Therefore, the model does not predict a highstand north of the Magdalena Delta because the ocean component (hydroisostasy) is negative. Conversely, the ice loading component is negative everywhere in northern South America (Milne et al., 2005 Fig. 5). This contrast relates to the dichotomy we are exploring: whether the ocean or ice loadings dominated during the Meghalayan age (–4.2 ka to present).

Considering the ocean-ice loadings dichotomy, SL indicators suggest contrasting origins. For example, the RSL highstands related to the ocean loading mechanism explain indicators in the southern Caribbean's marine terraces (Correa et al., 2007; Page, 1982). However, they do not concur with recent observations from coastal lagoons that suggest the dominance of the ice-loading effects (González, 2017; Khan et al., 2017; Urrego et al., 2013).

Since the SLE numerically solved by SELEN^4 is nonlinear, we cannot separate the ocean from ice loadings. However, we can distinguish them in the resulting SL curves to assess the intermediate- to far-field influence. First, results from the standard model align with the control of the ice loading (intermediate-field) mechanism north of our northernmost stations (e.g., Caribbean site 7, Guajira Peninsula, and site 5, Magdalena River Delta). There, the hydro-isostatic factor accounts for a mid-Northgrippian (–6 ka) RSL highstand in the order of centimeters. In other words, our northernmost stations are close to the southern limit of the intermediate-field effects from the Laurentide forebulge collapse. Thus, the ocean loading (far-field) effects are negligible in the northern Caribbean and more prominent in the south.

From our high viscosity model, representative of the Caribbean according to Milne and Peros (2013), we propose that the transition from far- to intermediate-field effects is located between the Gulf of Morrosquillo (site 3) and Manzanillo del Mar (site 4). As this result contradicts what is currently accepted by the scientific community (Khan et al., 2017), we respectfully highlight some pen slips that led to an incorrect interpretation of the Caribbean's SL indicators in previous works. The colleagues used two Caribbean records to calibrate a statistical model and concluded that intermediate-field effects dominate the Caribbean (Khan et al., 2017). However, one of the records corresponds to San Andres Island, located ~800 km from continental South America (González et al., 2010). This record hardly represents the RSL variability along the Caribbean coast of NW South

America. The second record corresponds to a coastal lagoon (Urrego et al., 2013), ~130 km NE from an emerged SL not considered due to tectonic “contamination” (Martínez et al., 2010). Considering the crustal block model, a question arises: why do we consider coastal lagoons as tectonically stable sites?

Furthermore, although not applied in the modeling, Khan et al. (2017) discussed the Pacific RSL record by Jaramillo and Bayona (2000) as a Caribbean SL indicator. According to our estimates and recent unpublished analyses (Gómez-Álvarez, 2022), the coastal lagoon records of Jaramillo and Bayona and Urrego et al. may lie in subsiding coastal fringes like other sectors along the Caribbean coast (e.g., Cartagena Bay) (Restrepo-Ángel et al., 2021). In this case, SL indicators are below modern mean SL by crustal block subsidence (see our discussion on tectonics).

With the standard viscosity model, we predict mid-Holocene (–6 ka) high-stands in the order of meters at the southern Caribbean and Pacific coasts that partially explain the emerged SL indicators. However, the model neither presents the submerged SL indicators nor their proximity to emerged indicators (e.g., Caribbean site 4 versus 5). Exploring the response of a 3D solid Earth structure might reconcile this inconsistency, as the GIA response would be linked to subduction styles and laterally heterogeneous rheology.

5.2. 3D Solid Earth Structure along Coastal Colombia

The influence of solid Earth’s rheology on postglacial GIA along the NW South America coast remains poorly understood. Optimizing solutions to the SL equation for the northern Caribbean with SL indicators in Cuba resulted in relatively high mantle viscosities (Milne and Peros, 2013). Given the spherically symmetric model of SELEN[4], we applied a similar mantle model in our VM5h simulations to represent the GIA response along the Caribbean coast (high viscosity), in contrast to the Pacific coast (standard-low viscosity) (e.g., Creveling et al., 2017). However, representing the complicated tectonic setting of NW South America may require a laterally varying, 3D solid Earth structure (Hay et al., 2017; Latychev et al., 2005; Mohammadzaheri et al., 2021). In the 3D case, the GIA response depends on lateral and vertical variations in crust thickness and mantle viscosity (Gomez et al., 2018; Thompson et al., 2023). In the far field, a 3D rheology implies variable controls of the gravitational and equatorial siphoning, with the continental levering relatively more influenced by local characteristics (Peak et al., 2022).

Considering the vertical rheology, northern South America exhibits a relatively thin crust of ~45 km (Feng et al., 2007) and three slabs with different subduction angles (Idárraga-García et al., 2016; Vargas and Mann, 2013). These features translate into low mantle viscosities along active plate boundaries with a steep subduction slab. Also, we expect high mantle viscosities along active plate boundaries with a shallower (flat) subduction slab. Global analogies include the high viscosity of the flat slab in Barbados (Austermann et al., 2013) and low viscosities in the active subduction zone of Alaska (Lange et al., 2014; Larsen et al., 2005).

A laterally variable mantle structure implies different relaxation times to surface load changes (Whitehouse, 2018). We expect such differences along the Pacific because of the latitudinally varying subduction: flat subduction south of Malpelo Island (Pacific site 3 near Naya River delta) and north of Solano Bay (Pacific site 5) and steep subduction centered at the San Juan River delta (Pacific sites 3 and 4) (Idárraga-García et al., 2016).

According to the subduction styles, the high mantle viscosity represents the Caribbean's flat slab and the Pacific subduction north of Solano Bay and south of the Naya River delta. Recent surface ice mass changes should influence the GIA response along these coasts. On the other hand, the low-viscosity model represents the steep-subduction region along the mid-Pacific coast. Emerged SL indicators by equatorial siphoning should dominate along these coasts.

5.3. Reconciling SL Indicators: The Role of Tectonics

Comparing RSL change simulations and SL indicators is customary as it can shed light on the role of tectonics (Garrett et al., 2020). Seminal studies in tectonically stable sites linked emerged landforms to postglacial hydro-isostatic effects. For example, in Australia, GIA explains mid-Holocene high stands of the order of meters if observations are used to adjust a mantle viscosity model (Nakada and Lambeck, 1989). These results agree with SL indicators in South America, e.g., the eastern coast of Brazil (Angulo et al., 2006) and the Rio de la Plata estuary (Prieto et al., 2017). Following the continental levering mechanism, these sites exhibit SL highstands >4 m (Mitrovica and Milne, 2002). For NW South America, previous works predicted a Holocene highstand of centimeters along the northern Caribbean coast, whereas predictions for the southern Caribbean proposed a ~3 m highstand (Clark et al., 1978; Page, 1982). Our results with the standard mantle structure concur with previous studies. On the other hand, results with the high viscosity model predict a stillstand south of the Gulf of Morrosquillo. Thus, in light of our results, tectonics are more significant than previously argued, especially on the southern Caribbean coast.

Active tectonics (including mud diapirism) shape the NW South American Caribbean coast with the interplay of three major tectonic plates, i.e., Caribbean, Nazca, and South American, and two main crustal blocks, i.e., Panamá-Chocó and Northern Andes (Cortés et al., 2005; Kellogg and Vega, 1995; Taboada et al., 2000). The shallow subduction of the Caribbean Plate beneath the South American Plate at 20 mm/a in the NE direction dominates coastal terrain deformation (Mora-Páez et al., 2019; Syracuse et al., 2016). These dynamics configure the Sinú-San Jacinto Deformed Belt in front of the subduction zone (cf. Figure 1). Four (2 to 5) of the seven analyzed sites are located within this deformational front.

The Gulf of Urabá (Caribbean site 1) is located on the eastern border of the Panamá-Chocó crustal block, at the limit of the Northern Andes Block. To the south, along the Atrato River valley, the Chocó block is limited by the Uramita and related faults, whereas to the north, these faults pass beneath the Gulf of Urabá and get dispersed within the Sinú Fold Belt and the North Panamá Thrust Belt. These active faults constitute thrust faults (with a minor left-lateral component) controlling the coastal zone's vertical deformation by subsidence and emergence.

Sites 2 to 5 (Minuto de Dios, Gulf of Morrosquillo, Manzanillo del Mar, and Magdalena River delta) are in the northern part of the Northern Andes Block, along the Sinú-San Jacinto Fold Belt. These terrains formed along folded sedimentary rocks imbricated with thrust faults and raised due to crust stacking (e.g., Vinnels et al., 2010). This deformation, which occurs along an extensive structure with many anisotropies, is poorly understood. However, the recent analyses along Cartagena Bay showed an RSL rise of ~7 mm/a linked to coastal subsidence by crustal block dynamics (Restrepo-Ángel et al., 2021). On the contrary, we can find the counterpart deformation that has produced coastal emergence at Manzanillo del Mar (Caribbean site 4, Figure 6D) (Martínez et al., 2010).

Considering GPS observations, preliminary analyses (Gómez-Álvarez, 2022) confirm the ~1 mm/a of subsidence at the Gulf of Morrosquillo proposed by previous unpublished reports (Page, 1982). Assuming subsidence operated uniformly during the Meghalayan (–4.2 ka to present), the SL indicators from González (2017) (Caribbean site 3) become +2.7 m at –4.3 ka and –0.4 m at –7.3 ka. These values concur with our standard model's –6 ka highstand (Figure 8A).

More pronounced than in the Caribbean, tectonics controls the coastal morphology in the Pacific through active faulting, mud diapirism, and co-seismic subsidence. The morphology controlled by tectonics includes: (1) active cliffs and short rivers with relatively low sediment load, on which subsidence levels determine lagoon/bay morphology; (2) inactive cliffs (bluffs) and hills, flanked by faults towards the littoral fringe; (3) the San Juan River delta, deposited on an oceanward dipping, gently-sloping graben; and (4) the Patia River delta, a deltaic region of co-seismic subsidence compartments (Correa, 1996, p. 149).

Overall, the alongshore succession of thrust faults, mud diapirism (Caribbean and Pacific), and co-seismic motions (Pacific) drive RSL change besides postglacial GIA. A variable continental level would result in a variable RSL change even for a relatively constant ocean level. We argue that these tectonic and structural responses provide the primary mechanism configuring RSL changes along the NW South American coast. In other words, contrary to what other studies suppose, none of the RSL indicators appear to result from a tectonically stable location.

5.4. What We Missed: Sediment Isostasy

A significant unknown in RSL change along the NW South American coast relates to sediment isostasy. Sediment deposition and erosion affect RSL change as it varies the mass distribution and relative distance between the ocean and solid Earth surfaces (Dalca et al., 2013). In NW South America, this distribution depends on sediment transfer to the continental shelf in the basin-coastal zone continuum. As sediment erodes from the continent, it would reduce continental mass and imply an RSL fall (by continental rising). On the contrary, sediment accumulation on the continent leads to mass loading and RSL rise.

Despite relatively few applications, available studies highlight sediment isostasy as an effective mechanism in RSL change for shelves with appreciable sediment input. Seminal analyses at Karachi in the Arabian Sea, close to the Indus Delta, proposed a postglacial RSL correction of ~7 m by sediment isostasy. This correction implies a Late Holocene stillstand instead of the highstand of ~3 m expected from ocean and ice loads (Ferrier et al., 2015, Fig. 6A).

Given the relatively large sediment load from Caribbean and Pacific catchments, the sediment isostasy promises to control RSL along NW South America. For example, fluvial sediment deposition has created arguably the most extensive delta systems along the Pacific Coast of North and South America (the Patia and San Juan River deltas) despite the narrow and high-energy shelf (Restrepo and López, 2008). Such delta progradation influences RSL by continental sediment redistribution (Dalca et al., 2013).

Another control in sediment isostasy is retention at floodplains. For example, floodplains prevent ~10% of fluvial sediment load from reaching the coastal zone in the depositional region (the Momposina Depression) within the Magdalena River catchment (Restrepo et al., 2006). Such deposition occurs on an area of ~25,000 km^2, translating into ~55 m of Holocene sediments (Latrubesse, 2015).

However, beyond floodplains, accumulation is complicated at NW South American deltas. For the Magdalena, jetties route fluvial sediments to the continental rise through a submarine canyon, preventing prodelta accumulation and shelf loading (Naranjo-Vesga et al., 2021). In this case, engineering structures modify delta morphodynamics, which results in increased channel siltation and an imbalance in marine sediment fluxes (Paniagua-Arroyave and Nienhuis, 2022; Restrepo et al., 2020). This imbalance varies sediment redistribution and prodelta reworking of Late Holocene deposits, adding another source of uncertainty to RSL changes.

In postglacial timescales (tens of thousands of years), sediment deposited in NW South American floodplains would lower RSL through continental tilting. On the contrary, RSL would rise by deposition on the continental shelf. A recent contribution suggests an RSL fall of ~15 m since the last interglacial (–122 ka) at deltas along the Caribbean and Pacific of NW South America due to sediment isostasy (Pico, 2020). Also, crustal uplift can be associated with erosional unloading via sediment isostasy and tectonic uplift, resulting in another source of RSL fall (Ruetenik et al., 2020).

6. Conclusions

Based on comparing postglacial relative sea-level change simulations (with a model that solves the gravitationally and topographically self-consistent sea-level equation and applies two mantle rheologies) to published sea-level indicators for NW South America's Caribbean and Pacific coasts, we find that:

- Far-field effects (equatorial siphoning and continental levering) have dominated along the Pacific coast during the Holocene, with highstands in the order of meters (–0.33 mm/a of Holocene relative sea-level fall).
- Intermediate-field effects (related to the Laurentide forebulge collapse) were more prominent along the Caribbean coast, with a late Holocene RSL rise in the north (+0.5 mm/a of Holocene relative sea-level change) and a standstill in the south (~0 mm/a).
- The change in influence between far- and intermediate-field effects occurs between the Gulf of Morrosquillo and Manzanillo del Mar along the Caribbean coast.
- The lateral variability in Earth's rheology supports applying a GIA model with 3D mantle structure, including the influence of sediment isostasy.
- According to the crustal blocks' approximation, published sea-level indicators correspond to emerged or submerged sites by faulting and folding, mud diapirism (Caribbean and Pacific), and co-seismic motions (Pacific).

Acknowledgments

J.F.P.A. acknowledges funding from the Vice-Presidency of Science, Technology, and Innovation at EAFIT University (award 952-000015), Florida State University Department of Earth, Ocean and Atmospheric Sciences, Utrecht University Department of Physical Geography, and the Polar Earth Observing Network (POLENET) and International Association of Cryospheric Sciences (IACS, to attend the 2019 Glacial Isostatic Adjustment Training School in Gavle, Sweden). The authors recognize supercomputing resources made available by *Centro de Computacion Científica Apolo* at EAFIT University (http://www.eafit.edu.co/apolo), with the gracious support of Juan G. Lalinde-Pulido, Laura Sánchez-Córdoba, and Jacobo Monsalve-Guzmán. The authors sincerely thank Glenn A. Milne for sharing his modeling results and guiding the comparison to sea-level indicators. J.F.P.A. acknowledges Iván D. Correa for inspiration and guidance regarding discussions of relative sea-level changes along coastal Colombia. The authors acknowledge thoughtful reviews by Barbara Mauz, Colin Murray-Wallace, and Juan L. Gonzalez on an earlier version of this manuscript and editorial work by Lewis Owen and Karin E. Perring. Supplemental information and data can be accessed at http://dx.doi.org/10.17632/7nhpbhvfnz.2. The authors declare that they have no known competing financial interests or personal relationships that could have appeared to influence the work reported in this paper. This work contributes to IGCP Project 725 'Forecasting Coastal Change'.

References

Anfuso, G., Postacchini, M., di Luccio, D., Benassai, G., 2021. Coastal sensitivity/vulnerability characterization and adaptation strategies: A review. J Mar Sci Eng 9, 1–29. https://doi.org/10.3390/jmse9010072

Angulo, R.J., Lessa, G.C., Souza, M.C. de, 2006. A critical review of mid- to late-Holocene sea-level fluctuations on the eastern Brazilian coastline. Quat Sci Rev 25, 486–506. https://doi.org/10.1016/j.quascirev.2005.03.008

Austermann, J., Mitrovica, J.X., Latychev, K., Milne, G.A., 2013. Barbados-based estimate of ice volume at Last Glacial Maximum affected by subducted plate. Nat Geosci 6, 553–557. https://doi.org/10.1038/NGEO1859

Bustamante, C., Archanjo, C.J., Cardona, A., Vervoort, J.D., 2016. Late Jurassic to Early Cretaceous plutonism in the Colombian Andes: A record of long-term arc maturity. Bulletin of the Geological Society of America 128, 1762–1779. https://doi.org/10.1130/B31307.1

Bustamante, C., Cardona, A., Restrepo, M., Zapata, D., Beltrán-Triviño, A., Bustamante, A., Valencia, V.A., 2023. Middle Triassic to Jurassic convergence at the north-western margin of Gondwana: insights from the Central Cordillera of Colombia. Int Geol Rev. https://doi.org/10.1080/00206814.2023.2195901

Carvajal, J.H., 2016. Mud Diapirism in the Central Colombian Caribbean Coastal Zone, in: Hermelin, M. (Ed.), Landscapes and Landforms of Colombia. Springer, Dordrecht, The Netherlands, pp. 35–53. https://doi.org/10.1007/978-3-319-11800-0_3

Cediel, F., Shaw, R.P., 2019. Geology and Tectonics of Northwestern South America. Springer International Publishing, Cham. https://doi.org/10.1007/978-3-319-76132-9

Clark, J.A., Farrell, W.E., Peltier, W.R., 1978. Global changes in postglacial sea level: A numerical calculation. Quat Res 9, 265–287. https://doi.org/10.1016/0033-5894(78)90033-9

Clark, P.U., Dyke, A.S., Shakun, J.D., Carlson, A.E., Clark, J., Wohlfarth, B., Mitrovica, J.X., Hostetler, S.W., McCabe, A.M., 2009. The Last Glacial Maximum. Science (1979) 325, 710–714.

Colmenares, L., Zoback, M.D., 2003. Stress field and seismotectonics of northern South America. Geology 31, 721–724.

Cooper, J.A.G., Meireles, R.P., Green, A.N., Klein, A.H.F., Toldo, E.E., 2018. Late Quaternary stratigraphic evolution of the inner continental shelf in response to sea-level change, Santa Catarina, Brazil. Mar Geol 397, 1–14. https://doi.org/10.1016/j.margeo.2017.11.011

Correa, I.D., 1996. Le Littoral Pacique Colombien: Interdependabce des Agents Morphostructuraux et Hydrodinamiques. PhD thesis, Universite Bordeaux I (Ph.D.). Universite Bordeaux I.

Correa, I.D., 1990. Inventario de erosión y acreción litoral (1793-1990) entre Los Morros y Galerazamba, Departamento de Bolívar, Colombia. Seminario Andino de Geología Ambiental 13, 129–144.

Correa, I.D., Acosta, S., Bedoya, G., 2007. Análisis de las Causas y Monitoreo de la Erosión Litoral en el Departamento de Córdoba. Fondo Editorial Universidad EAFIT, Medellin, Colombia.

Correa, I.D., Alcántara-Carrió, J., González R, D.A., 2005. Historical and recent shore erosion along the Colombian Caribbean coast. J Coast Res 52–57. https://doi.org/http://www.jstor.org/stable/25737404

Correa, I.D., Morton, R.A., 2010a. Caribbean Coast of Colombia, in: Bird, E.C.F. (Ed.), Encyclopedia of Coastal Landforms. Springer Science+Business Media, LLC, Dordrecht, The Netherlands, pp. 259–263.

Correa, I.D., Morton, R.A., 2010b. Pacific Coast of Colombia, in: Bird, E.C.F. (Ed.), Encyclopedia of Coastal Landforms. Springer Science+Business Media, LLC, Dordrecht, The Netherlands, pp. 193–197.

Correa, I.D., Paniagua-Arroyave, J.F., 2016. The Arboletes-Punta Rey Littoral, Southern Caribbean Coast, in: Hermelin, M. (Ed.), World Geomorphological Landscapes. Springer, Dordrecht, The Netherlands, pp. 55–63. https://doi.org/10.1007/978-3-319-11800-0_4

Correa, I.D., Pereira, C.I., 2019. The Historical, Geomorphological Evolution of the Colombian Littoral Zones (Eighteenth Century to Present), in: Cediel, F., Shaw, R.P. (Eds.), Geology and Tectonics of Northwestern South America. Springer, pp. 957–981. https://doi.org/10.1007/978-3-319-76132-9_16

Correa, I.D., Prüssmann-Uribe, J., Garrido-Escobar, A.E., 2016. Geomorfología del contorno litoral Urabá-Darién, departamentos de Antioquia y Chocó, Caribe Colombiano, in: Blanco-Libreros, J.F., Londoño-Mesa, M.H. (Eds.), Expedición Caribe Sur: Antioquia Y Chocó Costeros. Secretaría Ejecutiva de la Comisión Colombiana del Océano, Bogotá, Colombia, pp. 47–72.

Correa, I.D., Vernette, G., 2004. Introducción al problema de la erosión litoral en Urabá (sector Arboletes-Turbo) Costa Caribe colombiana. Boletín de Investigaciones Marinas y Costeras 33, 5–26.

Cortés, M., Angelier, J., Colletta, B., 2005. Paleostress evolution of the northern Andes (Eastern Cordillera of Colombia): Implications on plate kinematics of the South Caribbean region. Tectonics 24, 1–27. https://doi.org/10.1029/2003TC001551

Creveling, J.R., Mitrovica, J.X., Clark, P.U., Waelbroeck, C., Pico, T., 2017. Predicted bounds on peak global mean sea level during marine isotope stages 5a and 5c. Quat Sci Rev 163, 193–208. https://doi.org/10.1016/j.quascirev.2017.03.003

Dalca, A. v., Ferrier, K.L., Mitrovica, J.X., Perron, J.T., Milne, G.A., Creveling, J.R., 2013. On postglacial sea level-III. Incorporating sediment redistribution. Geophys J Int 194, 45–60. https://doi.org/10.1093/gji/ggt089

Dougherty, A.J., Thomas, Z.A., Fogwill, C., Hogg, A., Palmer, J., Rainsley, E., Williams, A.N., Ulm, S., Rogers, K., Jones, B.G., Turney, C., 2019. Redating the earliest evidence of the mid-Holocene relative sea-level highstand in Australia and implications for global sea-level rise. PLoS One 14, 1–19. https://doi.org/10.1371/journal.pone.0218430

Duque-Caro, H., 1990a. The Choco Block in the northwestern corner of South America: Structural, tectonostratigraphic, and paleogeographic implications. J South Am Earth Sci 3, 71–84.

Duque-Caro, H., 1990b. Neogene stratigraphy, paleoceanography and paleobiogeography in northwest South America and the evolution of the Panama Seaway. Palaeogeogr Palaeoclimatol Palaeoecol 77, 203–234.

Engelhart, S.E., Horton, B.P., 2012. Holocene sea level database for the Atlantic coast of the United States. Quat Sci Rev 54, 12–25. https://doi.org/10.1016/j.quascirev.2011.09.013

Engelhart, S.E., Horton, B.P., Douglas, B.C., Peltier, W.R., Törnqvist, T.E., 2009. Spatial variability of late Holocene and 20th century sea-level rise along the Atlantic coast of the United States. Geology 37, 1115–1118. https://doi.org/10.1130/G30360A.1

Engelhart, S.E., Horton, B.P., Kemp, A.C., 2011. Holocene Sea Level Changes Along the United States' Atlantic Coast. Oceanography 24, 70–79. https://doi.org/10.2307/24861269

Everts, C.H., 1987. Continental Shelf Evolution in Response to A Rise in Sea Level, in: Nummedal, D., Pilkey, O.H., Howard, J.D. (Eds.), Sea-Level Fluctuation and Coastal Evolution. SEPM Society for Sedimentary Geology Volume 41, Tulsa, OK, USA.

Farrell, W.E., Clark, J.A., 1976. On Postglacial Sea Level. Geophysical Journal of the Royal Astronomical Society 46, 647–667. https://doi.org/10.1111/j.1365-246X.1976.tb01252.x

Feng, M., van der Lee, S., Assumpção, M., 2007. Upper mantle structure of South America from joint inversion of waveforms and fundamental mode group velocities of Rayleigh waves. J Geophys Res Solid Earth 112, 1–16. https://doi.org/10.1029/2006JB004449

Ferrier, K.L., Mitrovica, J.X., Giosan, L., Clift, P.D., 2015. Sea-level responses to erosion and deposition of sediment in the Indus River basin and the Arabian Sea. Earth Planet Sci Lett 416, 12–20. https://doi.org/10.1016/j.epsl.2015.01.026

FitzGerald, D.M., Fenster, M.S., Argow, B.A., Buynevich, I. v., 2008. Coastal Impacts Due to Sea-Level Rise. Annu Rev Earth Planet Sci 36, 601–647. https://doi.org/10.1146/annurev.earth.35.031306.140139

Garrett, E., Melnick, D., Dura, T., Cisternas, M., Ely, L.L., Wesson, R.L., Jara-Muñoz, J., Whitehouse, P.L., 2020. Holocene relative sea-level change along the tectonically active Chilean coast. Quat Sci Rev 236. https://doi.org/10.1016/j.quascirev.2020.106281

Gomez, N., Latychev, K., Pollard, D., 2018. A coupled ice sheet-sea level model incorporating 3D earth structure: Variations in Antarctica during the Last Deglacial Retreat. J Clim 31, 4041–4054. https://doi.org/10.1175/JCLI-D-17-0352.1

Gómez-Álvarez, J.D., 2022. Geología estructural de la Bahía de Cartagena y su relación con los cambios relativos del nivel del mar. Tesis de Maestría en Ciencias de la Tierra, Universidad EAFIT (Master of Earth Sciences). Universidad EAFIT, Colombia, Medellin.

González, C., Urrego, L.E., Martínez, J.I., Polanía, J., Yokoyama, Y., 2010. Mangrove dynamics in the southwestern Caribbean since the "Little Ice Age": A history of human and natural disturbances. Holocene 20, 849–861. https://doi.org/10.1177/0959683610365941

González, J.L., 2017. How Far in the Caribbean does Forebulge induced subsidence extend? A new sea-level chronology from the tectonically stable central coast of Colombia. Geological Society of America Abstracts with Programs 49. https://doi.org/10.1130/abs/2017AM-303755

González, J.L., Correa, I.D., 2001. Late Holocene Evidence of Coseismic Subsidence on the San Juan Delta, Pacific Coast of Colombia. J Coast Res 17, 459–467.

González, J.L., Shen, Z., Mauz, B., 2014. New constraints on holocene uplift rates for the baudo mountain range, northwestern Colombia. J South Am Earth Sci 52, 194–202. https://doi.org/10.1016/j.jsames.2014.03.002

Gregory, J.M., Griffies, S.M., Hughes, C.W., Lowe, J.A., Church, J.A., Fukimori, I., Gomez, N., Kopp, R.E., Landerer, F., Cozannet, G. le, Ponte, R.M., Stammer, D., Tamisiea, M.E., van de Wal, R.S.W., 2019. Concepts and Terminology for Sea Level: Mean, Variability and Change, Both Local and Global. Surv Geophys 40, 1251–1289. https://doi.org/10.1007/s10712-019-09525-z

Hay, C.C., Lau, H.C.P., Gomez, N., Austermann, J., Powell, E., Mitrovica, J.X., Latychev, K., Wiens, D.A., 2017. Sea Level Fingerprints in a Region of Complex Earth Structure: The Case of WAIS. J Clim 30, 1881–1892. https://doi.org/10.1175/JCLI-D-16-0388.1

Hein, C.J., FitzGerald, D.M., de Menezes, J.T., Cleary, W.J., Klein, A.H.F., Albernaz, M.B., 2014. Coastal response to late-stage transgression and sea-level highstand. Bulletin of the Geological Society of America 126, 459–480. https://doi.org/10.1130/B30836.1

Idárraga-García, J., Kendall, J.M., Vargas, C.A., 2016. Shear wave anisotropy in northwestern South America and its link to the Caribbean and Nazca subduction geodynamics. Geochemistry, Geophysics, Geosystems 17, 3655–3673. https://doi.org/10.1002/2016GC006323

IGAC, INGEOMINAS, 2006. Investigación Integral del Andén Pacífico Colombiano, Tomo 1: Geología. Bogotá, Colombia.

Inman, D.L., Nordstrom, C.E., 1971. On the tectonic and morphologic classification of coasts. J Geol 79, 1–21.

Isla, F.I., 1989. Holocene sea-level fluctuation in the southern hemisphere. Quat Sci Rev 8, 359–368. https://doi.org/10.1016/0277-3791(89)90036-X

Jaramillo, C., Bayona, G., 2000. Mangrove distribution during the Holocene in Tribuga Gulf, Colombia. Biotropica 32, 14–22. https://doi.org/10.1111/j.1744-7429.2000.tb00443.x

Kellogg, J.N., Dixon, T.H., 1990. Central and South America GPS geodesy - CASA Uno. Geophys Res Lett 17, 195–198. https://doi.org/10.1029/GL017i003p00195

Kellogg, J.N., Vega, V., 1995. Tectonic Development of Panama, Costa Rica, and the Colombian Andes: Constraints from Global Positioning System Geodetic Studies and Gravity. Geological Society of America Special Paper 295, 75–90.

Kennedy, D.M., Oliver, T.S.N., Tamura, T., Murray-Wallace, C. v., Thom, B.G., Rosengren, N.J., Ierodiaconou, D., Augustinus, P., Leach, C., Gao, J., McSweeney, S.L., Konlechner, T., Woodroffe, C.D., 2020. Holocene evolution of the Ninety Mile Beach sand barrier, Victoria, Australia: The role of sea level, sediment supply and climate. Mar Geol 430, 106366. https://doi.org/10.1016/j.margeo.2020.106366

Khan, N.S., Ashe, E., Horton, B.P., Dutton, A., Kopp, R.E., Brocard, G., Engelhart, S.E., Hill, D.F., Peltier, W.R., Vane, C.H., Scatena, F.N., 2017. Drivers of Holocene sea-level change in the Caribbean. Quat Sci Rev 155, 13–36. https://doi.org/10.1016/j.quascirev.2016.08.032

Khan, N.S., Ashe, E., Shaw, T.A., Vacchi, M., Walker, J., Peltier, W.R., Kopp, R.E., Horton, B.P., 2015. Holocene Relative Sea-Level Changes from Near-, Intermediate-, and Far-Field Locations. Curr Clim Change Rep 1, 247–262. https://doi.org/10.1007/S40641-015-0029-Z

Khan, N.S., Horton, B.P., Engelhart, S., Rovere, A., Vacchi, M., Ashe, E.L., Törnqvist, T.E., Dutton, A., Hijma, M.P., Shennan, I., 2019. Inception of a global atlas of sea levels since the Last Glacial Maximum. Quat Sci Rev 220, 359–371. https://doi.org/10.1016/j.quascirev.2019.07.016

Kopp, R.E., Hay, C.C., Little, C.M., Mitrovica, J.X., 2015. Geographic Variability of Sea-Level Change. Curr Clim Change Rep. https://doi.org/10.1007/s40641-015-0015-5

Lambeck, K., Antonioli, F., Anzidei, M., Ferranti, L., Leoni, G., Scicchitano, G., Silenzi, S., 2011. Sea level change along the Italian coast during the Holocene and projections for the future. Quaternary International 232, 250–257. https://doi.org/10.1016/j.quaint.2010.04.026

Lange, H., Casassa, G., Ivins, E.R., Schröder, L., Fritsche, M., Richter, A., Groh, A., Dietrich, R., 2014. Observed crustal uplift near the Southern Patagonian Icefield constrains improved viscoelastic Earth models. Geophys Res Lett 41, 805–812. https://doi.org/10.1002/2013GL058419

Larsen, C.F., Motyka, R.J., Freymueller, J.T., Echelmeyer, K.A., Ivins, E.R., 2005. Rapid viscoelastic uplift in southeast Alaska caused by post-Little Ice Age glacial retreat. Earth Planet Sci Lett 237, 548–560. https://doi.org/10.1016/j.epsl.2005.06.032

Latrubesse, E.M., 2015. Large rivers, megafans and other Quaternary avulsive fluvial systems: A potential “who’s who” in the geological record. Earth Sci Rev. https://doi.org/10.1016/j.earscirev.2015.03.004

Latychev, K., Mitrovica, J.X., Tromp, J., Tamisiea, M.E., Komatitsch, D., Christara, C.C., 2005. Glacial isostatic adjustment on 3-D earth models: A finite-volume formulation. Geophys J Int 161, 421–444. https://doi.org/10.1111/j.1365-246X.2005.02536.x

Liu, J., Milne, G.A., Kopp, R.E., Clark, P.U., Shennan, I., 2015. Sea-level constraints on the amplitude and source distribution of Meltwater Pulse 1A. Nature Geoscience 2016 9:2 9, 130–134. https://doi.org/10.1038/ngeo2616

Liu, J.P., Milliman, J.D., 2004. Reconsidering melt-water pulses 1A and 1B: Global impacts of rapid sea-level rise. Journal of Ocean University of China 3, 183–190. https://doi.org/10.1007/s11802-004-0033-8

Lougheed, B.C., Obrochta, S.P., 2016. MatCal: Open Source Bayesian ^{14}C Age Calibration in Matlab. J Open Res Softw 4, 42. https://doi.org/10.5334/jors.130

Martínez, J.I., Yokoyama, Y., Gomez, A., Delgado, A., Matsuzaki, H., Rendon, E., 2010. Late Holocene marine terraces of the Cartagena region, southern Caribbean: The product of neotectonism or a former high stand in sea-level? J South Am Earth Sci 29, 214–224. https://doi.org/10.1016/j.jsames.2009.08.010

Martínez, J.O., López Ramos, E., 2010. High-resolution seismic stratigraphy of the late Neogene of the central sector of the Colombian Pacific continental shelf: A seismic expression of an active continental margin. J South Am Earth Sci 31, 28–44. https://doi.org/10.1016/j.jsames.2010.09.003

Melini, D., Spada, G., 2019. Some remarks on glacial isostatic adjustment modelling uncertainties. Geophys J Int 218, 401–413. https://doi.org/10.1093/gji/ggz158

Milne, G.A., Gehrels, W.R., Hughes, C.W., Tamisiea, M.E., 2009. Identifying the causes of sea-level change. Nat Geosci 2, 471–478. https://doi.org/10.1038/ngeo544

Milne, G.A., Long, A.J., Bassett, S.E., 2005. Modelling Holocene relative sea-level observations from the Caribbean and South America. Quat Sci Rev 24, 1183–1202. https://doi.org/10.1016/j.quascirev.2004.10.005

Milne, G.A., Mitrovica, J.X., 1998. Postglacial sea-level change on a rotating Earth. Geophys J Int 133, 1–19.

Milne, G.A., Peros, M., 2013. Data-model comparison of Holocene sea-level change in the circum-Caribbean region. Glob Planet Change 107, 119–131. https://doi.org/10.1016/j.gloplacha.2013.04.014

Mitrovica, J.X., Milne, G.A., 2002. On the origin of late Holocene sea-level highstands within equatorial ocean basins. Quat Sci Rev 21, 2179–2190. https://doi.org/10.1016/S0277-3791(02)00080-X

Mitrovica, J.X., Peltier, W.R., 1991. On postglacial geoid subsidence over the equatorial oceans. J Geophys Res 96. https://doi.org/10.1029/91jb01284

Mohammadzaheri, A., Sigloch, K., Hosseini, K., Mihalynuk, M.G., 2021. Subducted Lithosphere Under South America From Multifrequency P Wave Tomography. J Geophys Res Solid Earth 126. https://doi.org/10.1029/2020JB020704

Montes, C., Rodriguez-Corcho, A.F., Bayona, G., Hoyos, N., Zapata, S., Cardona, A., 2019. Continental margin response to multiple arc-continent collisions: The northern Andes-Caribbean margin. Earth Sci Rev 198, 102903. https://doi.org/10.1016/j.earscirev.2019.102903

Mora-Páez, H., Kellogg, J.N., Freymueller, J.T., 2020. Chapter 14 - Contributions of Space Geodesy for Geodynamic Studies in Colombia: 1988 to 2017, in: Gómez, J., Pinilla–Pachon, A.O. (Eds.), The Geology of Colombia - Volume 4 Quaternary. Servicio Geológico Colombiano, Bogotá, pp. 479–498. https://doi.org/10.32685/pub.esp.38.2019.14

Mora-Páez, H., Kellogg, J.N., Freymueller, J.T., Mencin, D., Fernandes, R.M.S., Diederix, H., LaFemina, P., Cardona-Piedrahita, L., Lizarazo, S., Peláez-Gaviria, J.R., Díaz-Mila, F., Bohórquez-Orozco, O., Giraldo-Londoño, L., Corchuelo-Cuervo, Y., 2019. Crustal deformation in the northern Andes – A new GPS velocity field. J South Am Earth Sci 89, 76–91. https://doi.org/10.1016/j.jsames.2018.11.002

Nakada, M., Lambeck, K., 1989. Late Pleistocene and Holocene sea-level change in the Australian region and mantle rheology. Geophys J Int 96, 497–517. https://doi.org/10.1111/j.1365-246X.1989.tb06010.x

Naranjo-Vesga, J., Ortiz-Karpf, A., Wood, L., Jobe, Z., Paniagua-Arroyave, J.F., Shumaker, L., Mateus-Tarazona, D., Galindo, P., 2020. Regional controls in the distribution and morphometry of deep-water gravitational deposits along a convergent tectonic margin. Southern caribbean of Colombia. Mar Pet Geol 121, 104639. https://doi.org/10.1016/j.marpetgeo.2020.104639

Naranjo-Vesga, J., Paniagua-Arroyave, J.F., Ortiz-Karpf, A., Wood, L., Jobe, Z., Galindo, P., Shumaker, L., Mateus-Tarazona, D., 2021. Controls on submarine canyon morphology along a convergent tectonic margin. The Southern Caribbean of Colombia. Mar Pet Geol 105493. https://doi.org/10.1016/j.marpetgeo.2021.105493

Nerem, R.S., Beckley, B.D., Fasullo, J.T., Hamlington, B.D., Masters, D., Mitchum, G.T., 2018. Climate-change–driven accelerated sea-level rise detected in the altimeter era. Proc Natl Acad Sci U S A 115, 2022–2025. https://doi.org/10.1073/pnas.1717312115

Nicholls, R.J., Cazenave, A., 2010. Sea-level rise and its impact on coastal zones. Science (1979). https://doi.org/10.1126/science.1185782

Nienhuis, J.H., Ashton, A.D., Edmonds, D.A., Hoitink, A.J.F., Kettner, A.J., Rowland, J.C., Törnqvist, T.E., 2020. Global-scale human impact on delta morphology has led to net land area gain. Nature 577, 514–518. https://doi.org/10.1038/s41586-019-1905-9

Nienhuis, J.H., Kim, W., Milne, G.A., Quock, M., Slangen, A.B.A., Törnqvist, T.E., 2023. River Deltas and Sea-Level Rise. Annu Rev Earth Planet Sci 51, 79–104. https://doi.org/10.1146/annurev-earth-031621

Nienhuis, J.H., van de Wal, R.S.W., 2021. Projections of Global Delta Land Loss From Sea-Level Rise in the 21st Century. Geophys Res Lett 48, 1–9. https://doi.org/10.1029/2021GL093368

Nygren, W.E., 1950. Bolivar Geosyncline of Northwestern South America. Bulletin of the American Association of Petroleum Geologists 34, 1998–2006.

Page, W.D., 1982. Tectonic Deformation of the Caribbean Coast Northwestern Colombia. San Francisco, CA, USA.

Page, W.D., James, M.E., 1981. Tectonic subsidence and evidence for the recurrence of large magnitude earthquakes near Bahía Solano, Colombia, in: Memorias III Congreso Colombiano de Geología1. pp. 14–20.

Paniagua-Arroyave, J.F., Iván D. Correa, Giorgio Anfuso, Peter N. Adams, 2018. Soft-Cliff Retreat in a Tropical Coast: The Minuto de Dios Sector, Caribbean Coast of Colombia. J Coast Res 81, 40. https://doi.org/10.2112/si81-006.1

Paniagua-Arroyave, J.F., Nienhuis, J.H., 2022. Global River Delta Morphology: Predictions Versus Observations within the Galloway Ternary Diagram. Authorea Preprints.

Passeri, D.L., Hagen, S.C., Medeiros, S.C., Bilskie, M. v., Alizad, K., Wang, D., 2015. The dynamic effects of sea level rise on low-gradient coastal landscapes: A review. Earths Future 3, 159–181. https://doi.org/10.1002/2015EF000298.Received

Pawlowicz, R., 2020. M_Map: A mapping package for MATLAB.

Peak, B.A., Latychev, K., Hoggard, M.J., Mitrovica, J.X., 2022. Glacial isostatic adjustment in the Red Sea: Impact of 3-D Earth structure. Quat Sci Rev 280, 107415. https://doi.org/10.1016/j.quascirev.2022.107415

Peltier, W.R., 2004. Global glacial isostasy and the surface of the ice-age Earth: The ICE-5G (VM2) model and GRACE. Annu Rev Earth Planet Sci. https://doi.org/10.1146/annurev.earth.32.082503.144359

Peltier, W.R., Argus, D.F., Drummond, R., 2015. Space geodesy constrains ice age terminal deglaciation: The global ICE-6G_C (VM5a) model. J Geophys Res Solid Earth 120, 450–487. https://doi.org/10.1002/2014JB011176

Peltier, W.R., Drummond, R., 2008. Rheological stratification of the lithosphere: A direct inference based upon the geodetically observed pattern of the glacial isostatic adjustment of the North American continent. Geophys Res Lett 35. https://doi.org/10.1029/2008GL034586

Pico, T., 2020. Towards assessing the influence of sediment loading on Last Interglacial sea level. Geophys J Int 220, 384–392. https://doi.org/10.1093/gji/ggz447

Pirazzoli, P.A., 1996. Sea-Level Changes: The Last 20,000 Years. John Wiley & Sons, Inc., Chichester, West Sussex, England.

Prieto, A.R., Mourelle, D., Peltier, W.R., Drummond, R., Vilanova, I., Ricci, L., 2017. Relative sea-level changes during the Holocene in the Río de la Plata, Argentina and Uruguay: A review. Quaternary International 442, 35–49. https://doi.org/10.1016/j.quaint.2016.02.044

Reimer, P.J., Reimer, R.W., 2001. A marine reservoir correction database and on-line interface. Radiocarbon 43, 461–463. https://doi.org/10.1017/s0033822200038339

Restrepo, J.C., Orejarena-Rondón, A., Consuegra, C., Pérez, J., Llinas, H., Otero, L., Álvarez, O., 2020. Siltation on a highly regulated estuarine system: The Magdalena River mouth case (Northwestern South America). Estuar Coast Shelf Sci 245. https://doi.org/10.1016/j.ecss.2020.107020

Restrepo, J.D., Kjerfve, B., Hermelin, M., Restrepo, J.C., 2006. Factors controlling sediment yield in a major South American drainage basin: The Magdalena River, Colombia. J Hydrol (Amst) 316, 213–232. https://doi.org/10.1016/j.jhydrol.2005.05.002

Restrepo, J.D., López, S.A., 2008. Morphodynamics of the Pacific and Caribbean deltas of Colombia, South America. J South Am Earth Sci 25, 1–21. https://doi.org/10.1016/j.jsames.2007.09.002

Restrepo, M., Bustamante, C., Cardona, A., Beltrán-Triviño, A., Bustamante, A., Chavarría, L., Valencia, V.A., 2021. Tectonic implications of the jurassic magmatism and the metamorphic record at the southern Colombian Andes. J South Am Earth Sci 111. https://doi.org/10.1016/j.jsames.2021.103439

Restrepo, M., Bustamante, C., Cardona, A., Beltrán-Triviño, A., Valencia, V.A., 2023. Geochemistry and geochronology of Permian plutonic rocks at the north-western margin of Gondwana. Geological Journal. https://doi.org/10.1002/gj.4743

Restrepo-Ángel, J.D., Mora-Páez, H., Díaz, F., Govorcin, M., Wdowinski, S., Giraldo-Londoño, L., Tosic, M., Fernández, I., Paniagua-Arroyave, J.F., Duque-Trujillo, J.F., 2021. Coastal subsidence increases vulnerability to sea level rise over 21st Century in Cartagena, Caribbean Colombia. Sci Rep.

Rovere, A., Stocchi, P., Vacchi, M., 2016. Eustatic and Relative Sea Level Changes. Curr Clim Change Rep. https://doi.org/10.1007/s40641-016-0045-7

Ruetenik, G.A., Ferrier, K.L., Creveling, J.R., Fox, M., 2020. Sea-level responses to rapid sediment erosion and deposition in Taiwan. Earth Planet Sci Lett 538, 116198. https://doi.org/10.1016/j.epsl.2020.116198

Shadrick, J.R., Rood, D.H., Hurst, M.D., Piggott, M.D., Hebditch, B.G., Seal, A.J., Wilcken, K.M., 2022. Sea-level rise will likely accelerate rock coast cliff retreat rates. Nat Commun 13, 7005. https://doi.org/10.1038/s41467-022-34386-3

Shennan, I., Long, A.J., Horton, B.P. (Eds.), 2015. Handbook of Sea-Level Research. John Wiley & Sons, Chichester, UK.

Spada, G., Melini, D., 2022. New estimates of ongoing sea level change and land movements caused by Glacial Isostatic Adjustment in the Mediterranean region. Geophys J Int 229, 984–998. https://doi.org/10.1093/gji/ggab508

Spada, G., Melini, D., 2019. SELEN4 (SELEN version 4.0): a Fortran program for solving the gravitationally and topographically self-consistent Sea Level Equation in Glacial Isostatic Adjustment modeling. Geosci Model Dev 12, 5055–5075. https://doi.org/m10.5194/gmd-12-5055-2019

Syracuse, E.M., Maceira, M., Prieto, G.A., Zhang, H., Ammon, C.J., 2016. Multiple plates subducting beneath Colombia, as illuminated by seismicity and velocity from the joint inversion of seismic and gravity data. Earth Planet Sci Lett 444, 139–149. https://doi.org/10.1016/J.EPSL.2016.03.050

Taboada, A., Rivera, L.A., Fuenzalida, A., Cisternas, A., Philip, H., Bijwaard, H., Olaya, J., Rivera, C., 2000. Geodynamics of the northern Andes: Subductions and intracontinental deformation (Colombia). Tectonics 19, 787–813. https://doi.org/10.1029/2000TC900004

Tegmark, M., 1996. An icosahedron-based method for pixelizing the celestial sphere. Astrophys J 470, L81–L84.

Thompson, S.B., Creveling, J.R., Latychev, K., Mitrovica, J.X., 2023. Three-dimensional glacial isostatic adjustment modeling reconciles conflicting geographic trends in North American marine isotope stage 5a relative sea level observations. Geology. https://doi.org/10.1130/G51257.1

Törnqvist, T.E., Jankowski, K.L., Li, Y.X., González, J.L., 2020. Tipping points of Mississippi Delta marshes due to accelerated sea-level rise. Sci Adv 6. https://doi.org/10.1126/sciadv.aaz5512

Urrego, L.E., Correa-Metrio, A., González, C., Castaño, A.R., Yokoyama, Y., 2013. Contrasting responses of two Caribbean mangroves to sea-level rise in the Guajira Peninsula (Colombian Caribbean). Palaeogeogr Palaeoclimatol Palaeoecol 370, 92–102. https://doi.org/10.1016/j.palaeo.2012.11.023

Vargas, C.A., Mann, P., 2013. Tearing and breaking off of subducted slabs as the result of collision of the panama arc-indenter with Northwestern South America. Bulletin of the Seismological Society of America 103, 2025–2046. https://doi.org/10.1785/0120120328

Vélez, M.I., Escobar, J., Brenner, M., Rangel, O., Betancourt, A., Jaramillo, A.J., Curtis, J.H., Moreno, J.L., 2014. Middle to late Holocene relative sea level rise, climate variability and environmental change along the Colombian Caribbean coast. Holocene 24, 898–907. https://doi.org/10.1177/0959683614534740

Vernette, G., Mauffret, A., Bobier, C., Briceno, L., Gayet, J., 1992. Mud diapirism, fan sedimentation and strike-slip faulting, Caribbean Colombian Margin. Tectonophysics 202, 335–349.

Vinnels, J.S., Butler, R.W.H., McCaffrey, W.D., Paton, D.A., 2010. Depositional processes across the Sinú Accretionary Prism, offshore Colombia. Mar Pet Geol 27, 794–809. https://doi.org/10.1016/j.marpetgeo.2009.12.008

Vivas-Narváez, A., 2019. Caracterización y Amenaza de los Volcanes de Lodo en los Municipios de Turbo, Necoclí, San Juan de Urabá y Arboletes. Corporación para el Desarrollo Sostenible del Urabá (Corpourabá).

Walker, M., Head, M.J., Berkelhammer, M., Björck, S., Cheng, H., Cwynar, L., Fisher, D., Gkinis, V., Long, A., Lowe, J., Newnham, R., Rasmussen, S.O., Weiss, H., 2018. Formal ratification of the subdivision of the Holocene Series/ Epoch (Quaternary System/Period): Two new Global Boundary Stratotype Sections and Points (GSSPs) and three new stages/ subseries. Episodes 41, 213–223. https://doi.org/10.18814/epiiugs/2018/018016

Whitehouse, P.L., 2018. Glacial isostatic adjustment modelling: Historical perspectives, recent advances, and future directions. Earth Surface Dynamics 6, 401–429. https://doi.org/10.5194/ESURF-6-401-2018

Yokoyama, Y., Purcell, A., 2021. On the geophysical processes impacting palaeo-sea-level observations. Geosci Lett. https://doi.org/10.1186/s40562-021-00184-w

Figures

Figure 1. Study location geology and tectonics, (A) in South America, and (B) general geology and tectonics of northern South America (black box in panel A), including plate boundaries, faults, fault systems (letters), and primary tectonic affinities (colors). Modified from Montes et al. (2019) and Mora-Paez et al. (2019). Plate motions relative to the North Andean Block with slip rates in cm/yr after Kellogg and Dixon (1990). Block velocity relative to the stable North Andean Block (1 cm/yr) from Mora-Páez et al. (2020). Coastline data (Panel A) from the Global Self-consistent, Hierarchical, High-resolution Geography Database (GSHHG) from the M_Map routine (Pawlowicz, 2020).

Figure 2. Coastal geomorphology, including main cities and sea-level indicators along the Caribbean coast of NW South America. Note the location of cliffs, shore platforms, and paleo cliffs (emerged terraces) in concordance with tectonic affinities (e.g., Arboletes). Beaches, beach ridges, etc., can be found elsewhere (e.g., the Atrato River delta). Geomorphology data from Correa and Pereira (2019 Fig. 2). Coastline data from the Global Self-consistent, Hierarchical, High-resolution Geography Database (GSHHG) and elevation data from the ETOPO1 1 arc-minute global relief model, both from the M_Map routine (Pawlowicz, 2020).

Figure 3. Coastal geomorphology, including main cities, major earthquakes, and sea-level indicators along the Pacific coast of NW South America. Note the location of cliffs, shore platforms, and paleo cliffs (emerged terraces) in concordance with tectonic affinities (e.g., Juradó). Beaches, etc., are found elsewhere (e.g., the Mira River Delta). Seven earthquakes are registered with Mw>7.0 (orange circles with black numbers; please see our Supplemental Information at http://dx.doi.org/10.17632/7nhpbhvfnz.2 for details). Earthquakes from U.S. Geological Survey's app "Latest Earthquakes" v.1.3.1 (https://earthquake.usgs.gov/). Geomorphology from Correa and Pereira (2019 Fig. 12). Coastline data from the GSHHG Database and elevation data from the ETOPO1 1 model, both from the M_Map routine (Pawlowicz, 2020).

Figure 4. Location of relative sea-level sites along Colombia's Caribbean Coast (red circles). Coastline data from the Global Self-consistent, Hierarchical, High-resolution Geography Database (GSHHG) and elevation data from ETOPO1 1 arc-minute global relief model, both from the M_Map routine (Pawlowicz, 2020). Note that the selection of these sites is arbitrary, following the general location of SL indicators and landmarks.

Figure 5. Location of relative sea-level sites along Colombia's Pacific Coast (blue diamonds). Coastline data from the Global Self-consistent, Hierarchical, High-resolution Geography Database (GSHHG) and elevation data from ETOPO1 1 arc-minute global relief model, both from the M_Map routine (Pawlowicz, 2020). Note that the selection of these sites is arbitrary, following the general location of SL indicators and landmarks.

Figure 6. Modeled relative sea-level curves from SELEN^4 for the two mantle viscosity scenarios (VM5i, standard mantle viscosity, light red; and VM5h, high mantle viscosity, dark red) for locations along the Caribbean Coast of Colombia (A) since the Last Glacial Maximum and (B) Holocene (–11.7 ka to present, Walker et al., 2018). Dashed lines mark age transitions within the Holocene epoch at –8.236 ka (Greenlandian-Northgrippian) and –4.2 ka (Northgrippian-Meghalayan).

Figure 7. Modeled relative sea-level curves from SELEN^4 for the two mantle viscosity scenarios (VM5i, standard mantle viscosity, light blue; and VM5h, high mantle viscosity, dark blue) for locations along the Pacific Coast of Colombia (A) since the Last Glacial Maximum and (B) Holocene (–11.7 ka to present, Walker et al., 2018). Dashed lines mark age transitions within the Holocene epoch at –8.236 ka (Greenlandian-Northgrippian) and –4.2 ka (Northgrippian-Meghalayan).

Figure 8. Modeled relative sea-level curves during the Late Holocene (–8.236 ka to present) for locations along the Colombian Caribbean Coast: (A) Standard viscosity scenario, VM5i (light red), and (B) High viscosity scenario, VM5h (dark red). The vertical dashed line shows the Northgrippian-Meghalayan age transition at –4.2 ka.

Figure 9. Modeled relative sea-level curves during the Late Holocene (–8.236 ka to present) for the Colombian Pacific Coast: (A) Standard viscosity scenario, VM5i, and (B) High viscosity scenario, VM5h. The vertical dashed line shows the Northgrippian-Meghalayan transition at –4.2 ka.

Figure 10. Comparison between modeling results and sea-level indicators from the literature for the Caribbean coast of NW South America (González, 2017; Martínez et al., 2010; Page, 1982; Urrego et al., 2013; Vélez et al., 2014) (please see our Supplemental Information at http://dx.doi.org/10.17632/7nhpbhvfnz.2). (A) Location of sea-level indicators (gray triangles) indicating the subplot in black letters; simulated RSL curves for VM5i and VM5h models for (B) site 2 near Minuto de Dios; (C) site 3 near the Gulf of Morrosquillo; (D) site 4 near Manzanillo del Mar; (E) site 5 near the Magdalena River delta; (F) site 6 near the Ranchería river delta. All dates have 1950 AD as the Time 0 ka (present). Vertical dashed lines indicate the Northgrippian-Meghalayan transition at –4.2 ka. We distinguish between index points and marine limiting date indicators following Khan et al. (2017) and references therein.

Figure 11. Comparison between our modeling results and sea-level indicators from the literature for the Pacific coast of NW South America (González et al., 2014; Jaramillo & Bayona, 2000; Page & James, 1981) (data in our Supplemental Information at http://dx.doi.org/10.17632/7nhpbhvfnz.2). (A) Location of sea-level indicators (gray triangles) with letters indicating the subplot in black letters; simulated RSL curves for VM5i and VM5h models for (B) site 5 near Bajo Baudó; (C) site 6 near Utría Cove; and (D) site 7 near Solano Bay. We distinguish between index points and marine limiting date indicators following Khan et al. (2017) and references therein.

Tables

Table 1. Relative sea-level curve locations (geographical coordinates) for SELEN^4 simulations for the Northwestern South American coast. These locations are arbitrarily selected according to geographical landmarks (e.g., deltas, bays, etc.). Some sites include nearby large cities and towns between dashes and in italics for reference (e.g., Minuto de Dios near Arboletes town).

Table 2. Profiles of density, rigidity, and viscosity for the VM5i (standard mantle viscosity) model. LT: lithosphere, UM: upper mantle, TZ: transition zone, LM: lower mantle, and CO: core. Rheological parameters after Spada and Melini (2019).

Table 3. Profiles of density, rigidity, and viscosity for the VM5h (high mantle viscosity) model. LT: lithosphere, UM: upper mantle, TZ: transition zone, LM: lower mantle, and CO: core. We propose the viscosity profile after Milne and Peros (2013) and Milne et al. (2005).

Tables

Table 1. Relative sea-level curve locations (geographical coordinates) for SELEN[4] simulations for the Northwestern South American coast. These locations are arbitrarily selected according to geographical landmarks (e.g., deltas, bays, etc.). Some sites include nearby large cities and towns between dashes and in italics for reference (e.g., Minuto de Dios near Arboletes town).

Site	Latitude	Longitude	Location
Caribbean Coast			
1	8.623	-77.125	Gulf of Urabá entrance
2	8.880	-76.425	Minuto de Dios -*Arboletes*-
3	9.528	-75.635	Gulf of Morrosquillo -*Coveñas*-
4	10.512	-75.514	Manzanillo del Mar -*Cartagena*-
5	11.235	-74.925	Magdalena River Delta -*Barranquilla*-
6	11.572	-72.923	Ranchería River Delta -*Riohacha*-
7	12.375	-71.900	Guajira Peninsula
Pacific Coast			
1	1.668	-79.131	Mira River Delta -*Tumaco*-
2	2.776	-78.717	Patía River Delta -*Guapi*-
3	3.265	-77.610	Naya River Delta
4	4.038	-77.660	San Juan River Delta -*Buenaventura*-
5	5.314	-77.441	Bajo Baudó
6	6.000	-77.400	Utría Cove -*Bahía Solano*-
7	6.342	-77.447	Solano Bay -*Bahía Solano*-
8	7.067	-77.793	Juradó

Tables

Table 2. Profiles of density, rigidity, and viscosity for the VM5i (standard mantle viscosity) model. LT: lithosphere, UM: upper mantle, TZ: transition zone, LM: lower mantle, and CO: core. Rheological parameters after Spada and Melini (2019).

Lower radius (m)	Upper radius (m)	Thickness (km)	Density (kg/m^3)	Rigidity (Pa)	Viscosity (Pa.s)	Layer
6,281,000	6,371,000	90	3,192.80	5.96E+10	1.0E+30	LT
6,151,000	6,281,000	130	3,369.06	6.67E+10	5.0E+20	UM1
5,971,000	6,151,000	180	3,475.58	7.64E+10	5.0E+20	UM2
5,701,000	5,971,000	270	3,857.75	1.06E+11	5.0E+20	TZ
5,401,000	5,701,000	300	4,446.25	1.70E+11	3.2E+21	LM1
5,072,933	5,401,000	328	4,615.83	1.91E+11	3.2E+21	LM2
4,716,800	5,072,933	356	4,813.85	2.12E+11	3.2E+21	LM3
4,332,600	4,716,800	384	4,997.86	2.33E+11	3.2E+21	LM4
3,920,333	4,332,600	412	5,202.00	2.55E+11	3.2E+21	LM5
3,480,000	3,920,333	440	5,408.57	2.79E+11	3.2E+21	LM6
0	3,480,000	3,480	10,931.73	0.00E+00	0.0E+00	CO

Tables

Table 3. Profiles of density, rigidity, and viscosity for the VM5h (high mantle viscosity) model. LT: lithosphere, UM: upper mantle, TZ: transition zone, LM: lower mantle, and CO: core. We propose the viscosity profile after Milne and Peros (2013) and Milne et al. (2005).

Lower radius (m)	Upper radius (m)	Thickness (km)	Density (kg/m^3)	Rigidity (Pa)	Viscosity (Pa.s)	Layer
6,281,000	6,371,000	90	3,192.80	5.96E+10	1.0E+30	LT
6,151,000	6,281,000	130	3,369.06	6.67E+10	5.0E+20	UM1
5,971,000	6,151,000	180	3,475.58	7.64E+10	5.0E+20	UM2
5,701,000	5,971,000	270	3,857.75	1.06E+11	5.0E+20	TZ
5,401,000	5,701,000	300	4,446.25	1.70E+11	3.0E+22	LM1
5,072,933	5,401,000	328	4,615.83	1.91E+11	3.0E+22	LM2
4,716,800	5,072,933	356	4,813.85	2.12E+11	3.0E+22	LM3
4,332,600	4,716,800	384	4,997.86	2.33E+11	3.0E+22	LM4
3,920,333	4,332,600	412	5,202.00	2.55E+11	3.0E+22	LM5
3,480,000	3,920,333	440	5,408.57	2.79E+11	3.0E+22	LM6
0	3,480,000	3,480	10,931.73	0.00E+00	0.0E+00	CO

Fig. 1

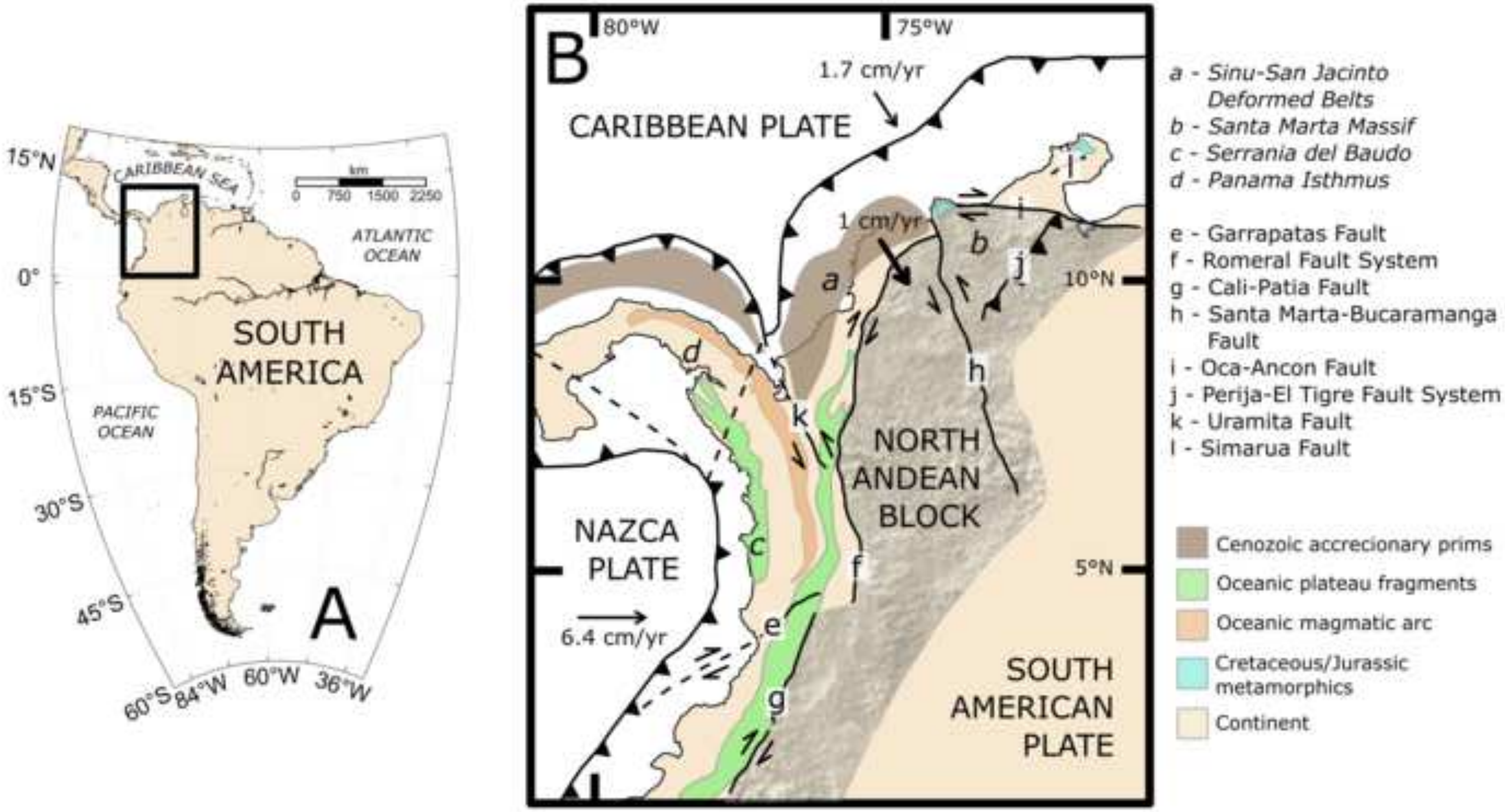
15°N
CARIBBEAN SEA
km
0 750 1500 2250
ATLANTIC OCEAN
0°
SOUTH AMERICA
15°S
PACIFIC OCEAN
30°S
45°S
60°S
84°W
60°W
36°W
A
B
80°W
75°W
1.7 cm/yr
CARIBBEAN PLATE
1 cm/yr
a
b
c
d
e
f
g
h
i
j
k
l
10°N
5°N
NORTH ANDEAN BLOCK
NAZCA PLATE
6.4 cm/yr
SOUTH AMERICAN PLATE
a - Sinu-San Jacinto Deformed Belts
b - Santa Marta Massif
c - Serrania del Baudo
d - Panama Isthmus
e - Garrapatas Fault
f - Romeral Fault System
g - Cali-Patia Fault
h - Santa Marta-Bucaramanga Fault
i - Oca-Ancon Fault
j - Perija-El Tigre Fault System
k - Uramita Fault
l - Simarua Fault
Cenozoic accrecionary prims
Oceanic plateau fragments
Oceanic magmatic arc
Cretaceous/Jurassic metamorphics
Continent

Fig. 2

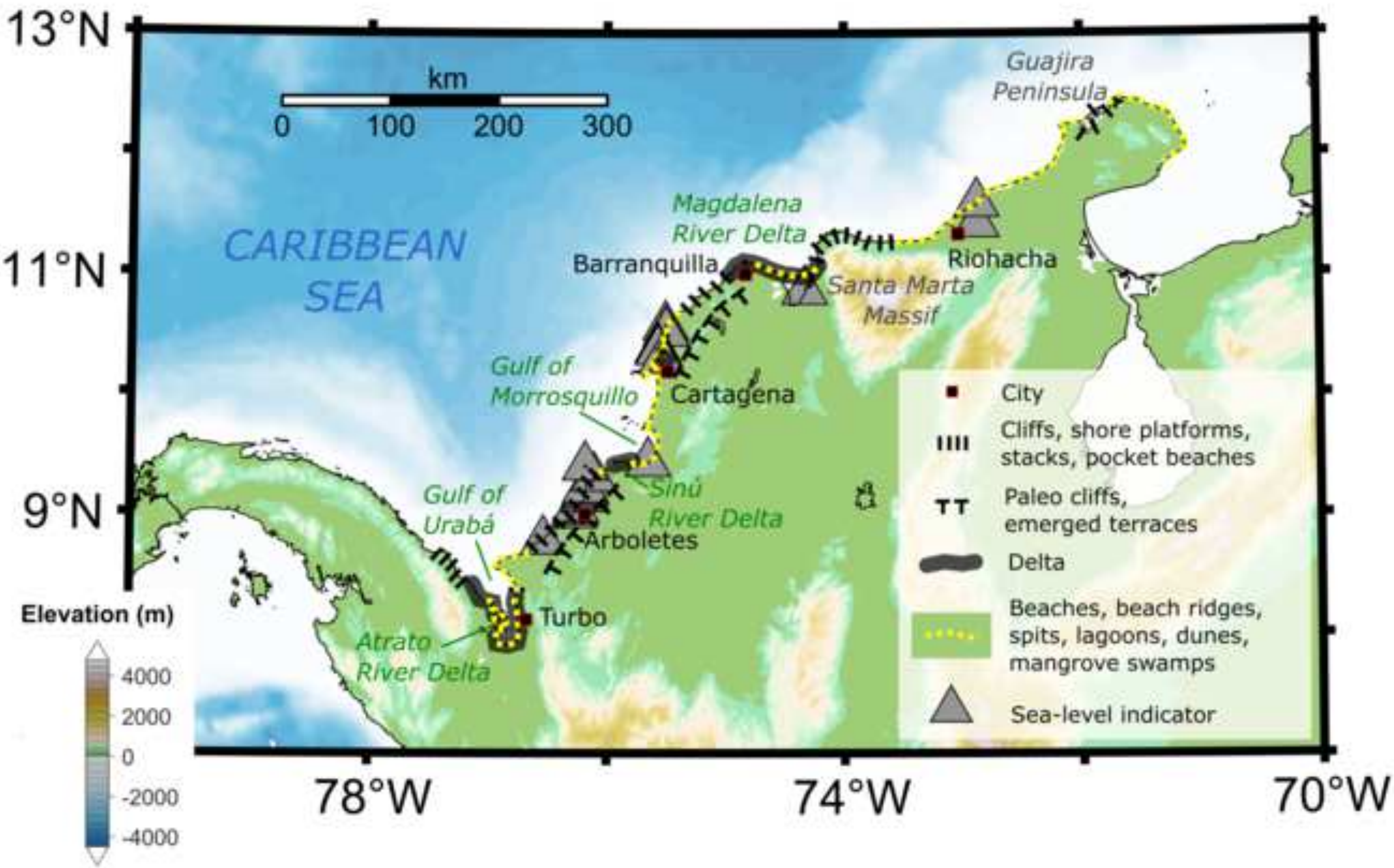
13°N
11°N
9°N
78°W
74°W
70°W
km
0
100
200
300
CARIBBEAN SEA
Guajira Peninsula
Magdalena River Delta
Barranquilla
Riohacha
Santa Marta Massif
Gulf of Morrosquillo
Cartagena
Gulf of Urabá
Sinú River Delta
Arboletes
Turbo
Atrato River Delta
Elevation (m)
4000
2000
0
-2000
-4000
City
Cliffs, shore platforms, stacks, pocket beaches
Paleo cliffs, emerged terraces
Delta
Beaches, beach ridges, spits, lagoons, dunes, mangrove swamps
Sea-level indicator

Fig. 3

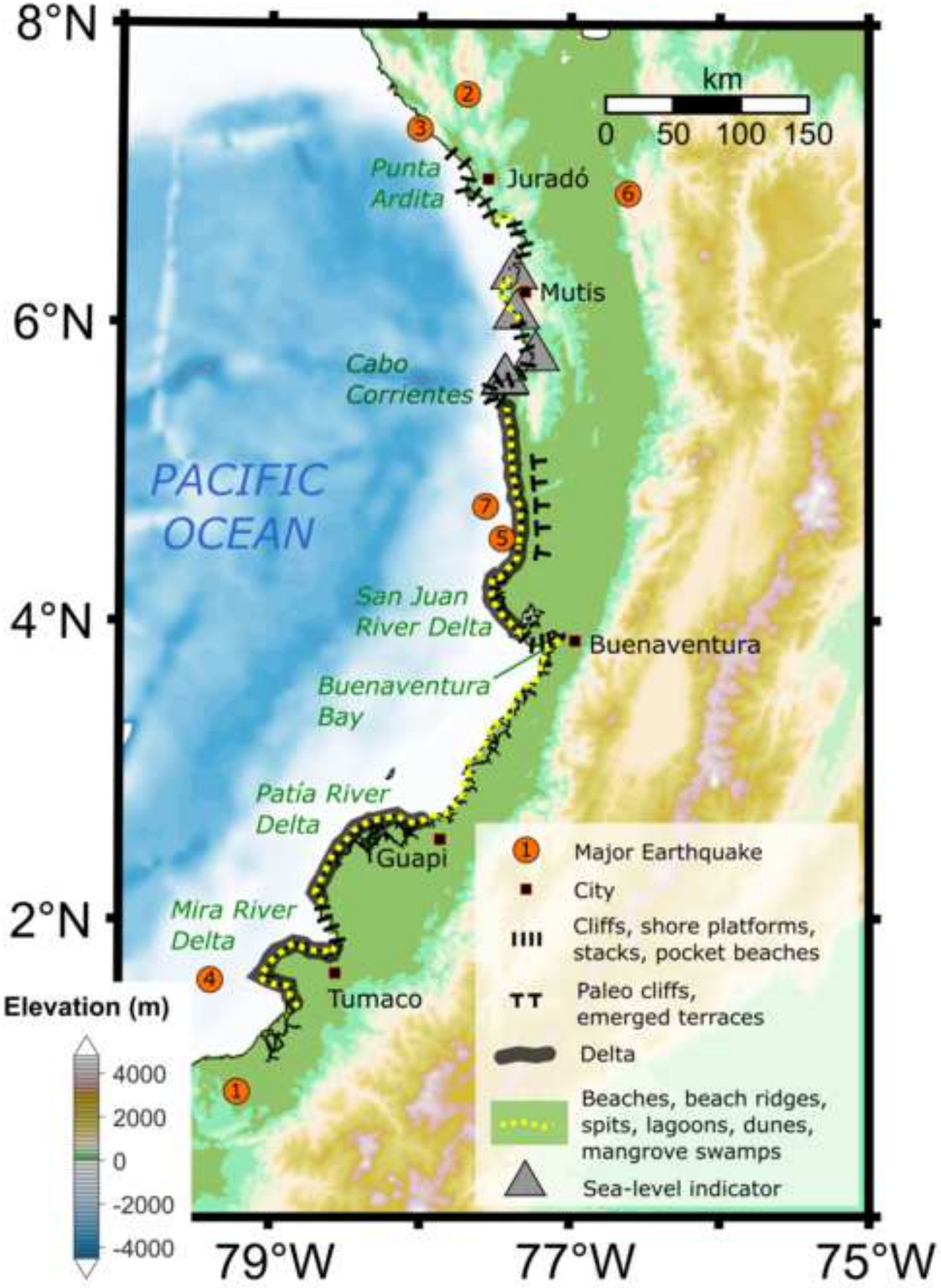
8°N
6°N
4°N
2°N
79°W
77°W
75°W
km
0 50 100 150
PACIFIC OCEAN
Punta Ardita
Juradó
Mutís
Cabo Corrientes
San Juan River Delta
Buenaventura
Buenaventura Bay
Patía River Delta
Guapi
Mira River Delta
Tumaco
1
2
3
4
5
6
7
Elevation (m)
4000
2000
0
-2000
-4000
Major Earthquake
City
Cliffs, shore platforms, stacks, pocket beaches
Paleo cliffs, emerged terraces
Delta
Beaches, beach ridges, spits, lagoons, dunes, mangrove swamps
Sea-level indicator

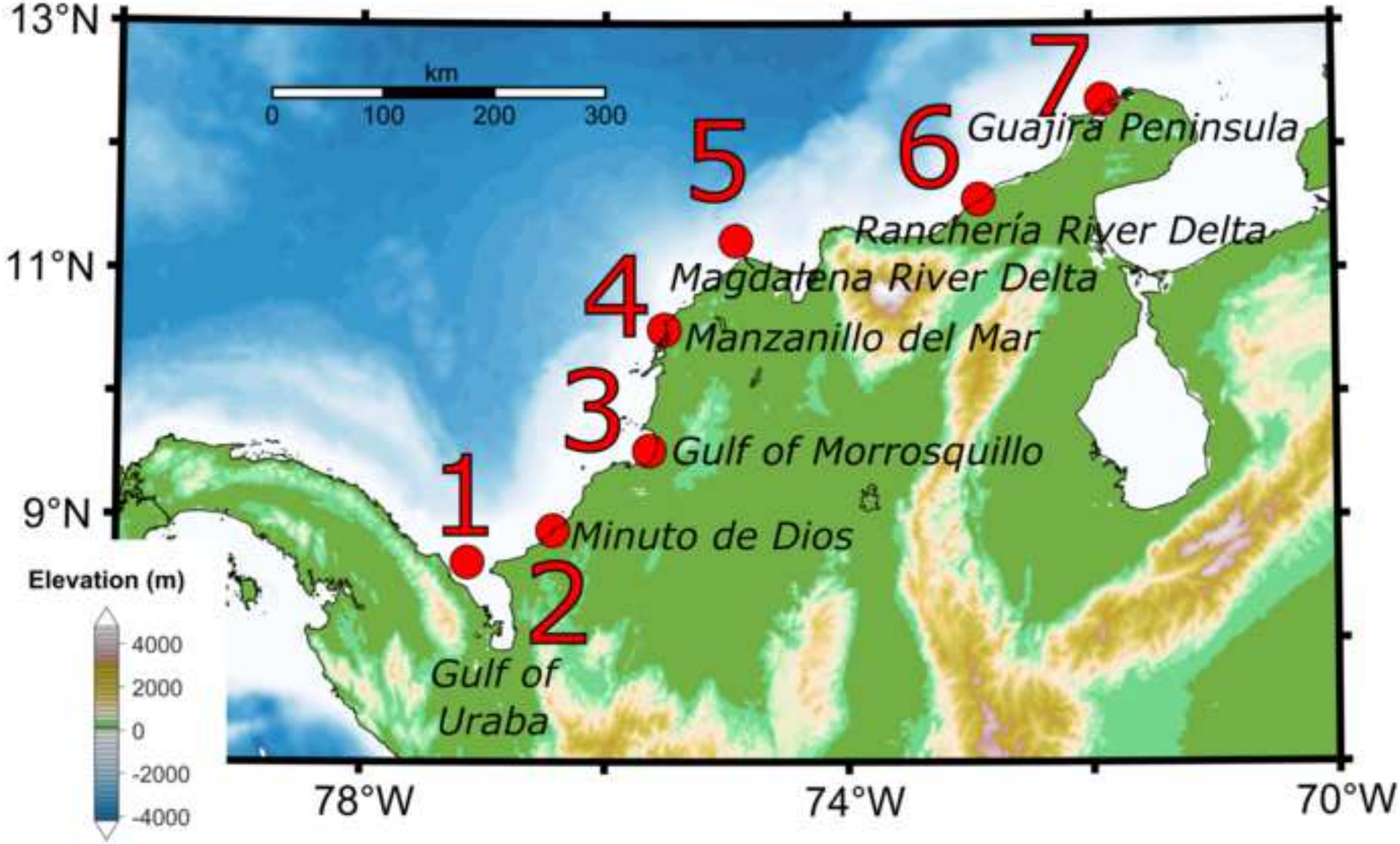
13°N
11°N
9°N
78°W
74°W
70°W
km
0
100
200
300
1
2
3
4
5
6
7
Gulf of Uraba
Minuto de Dios
Gulf of Morrosquillo
Manzanillo del Mar
Magdalena River Delta
Ranchería River Delta
Guajira Peninsula
Elevation (m)
4000
2000
0
-2000
-4000

Fig. 5

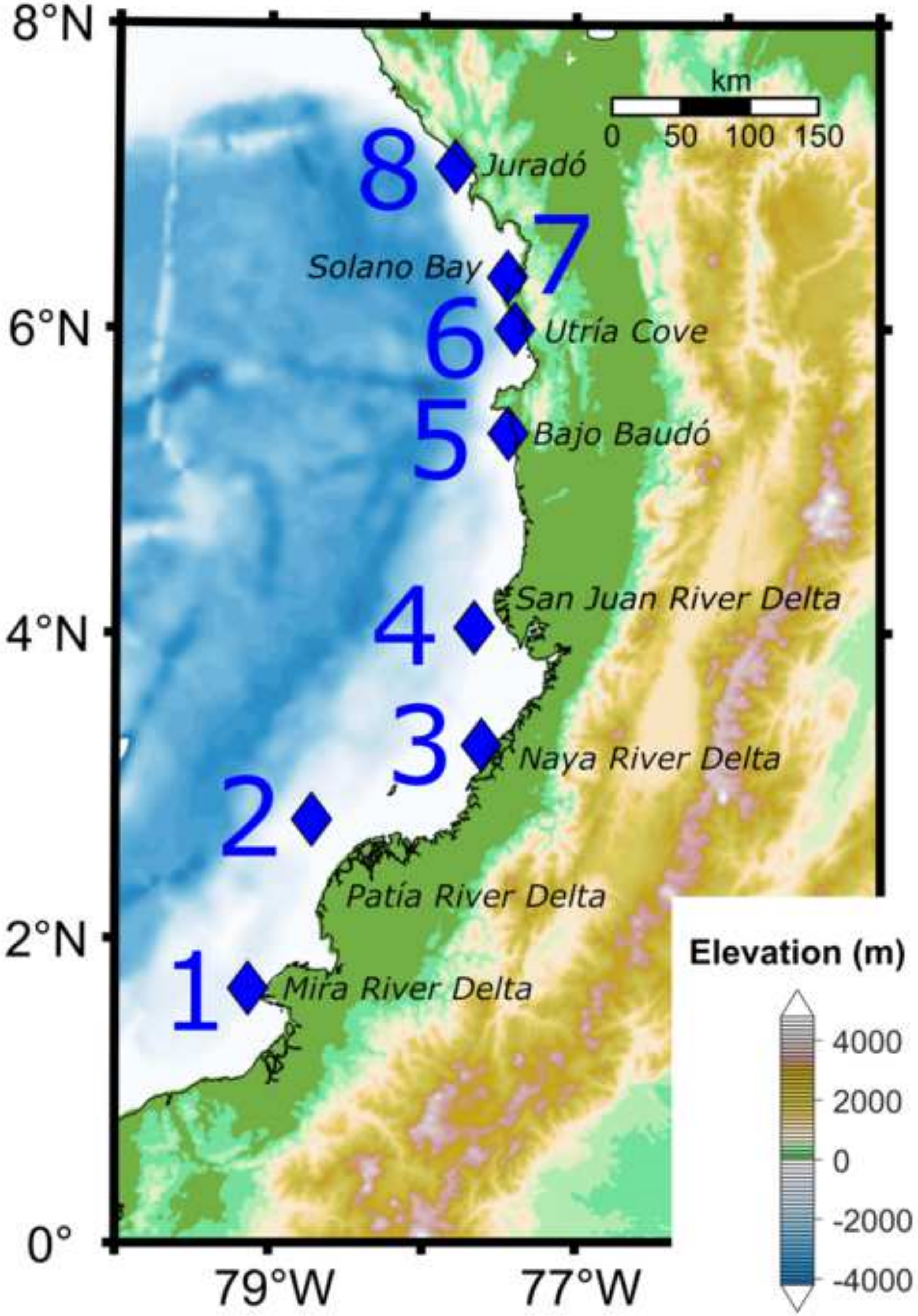
8°N
6°N
4°N
2°N
0°
79°W
77°W
km
0
50
100
150
8
Juradó
7
Solano Bay
6
Utría Cove
5
Bajo Baudó
San Juan River Delta
4
3
Naya River Delta
2
Patía River Delta
1
Mira River Delta
Elevation (m)
4000
2000
0
-2000
-4000

Fig. 6

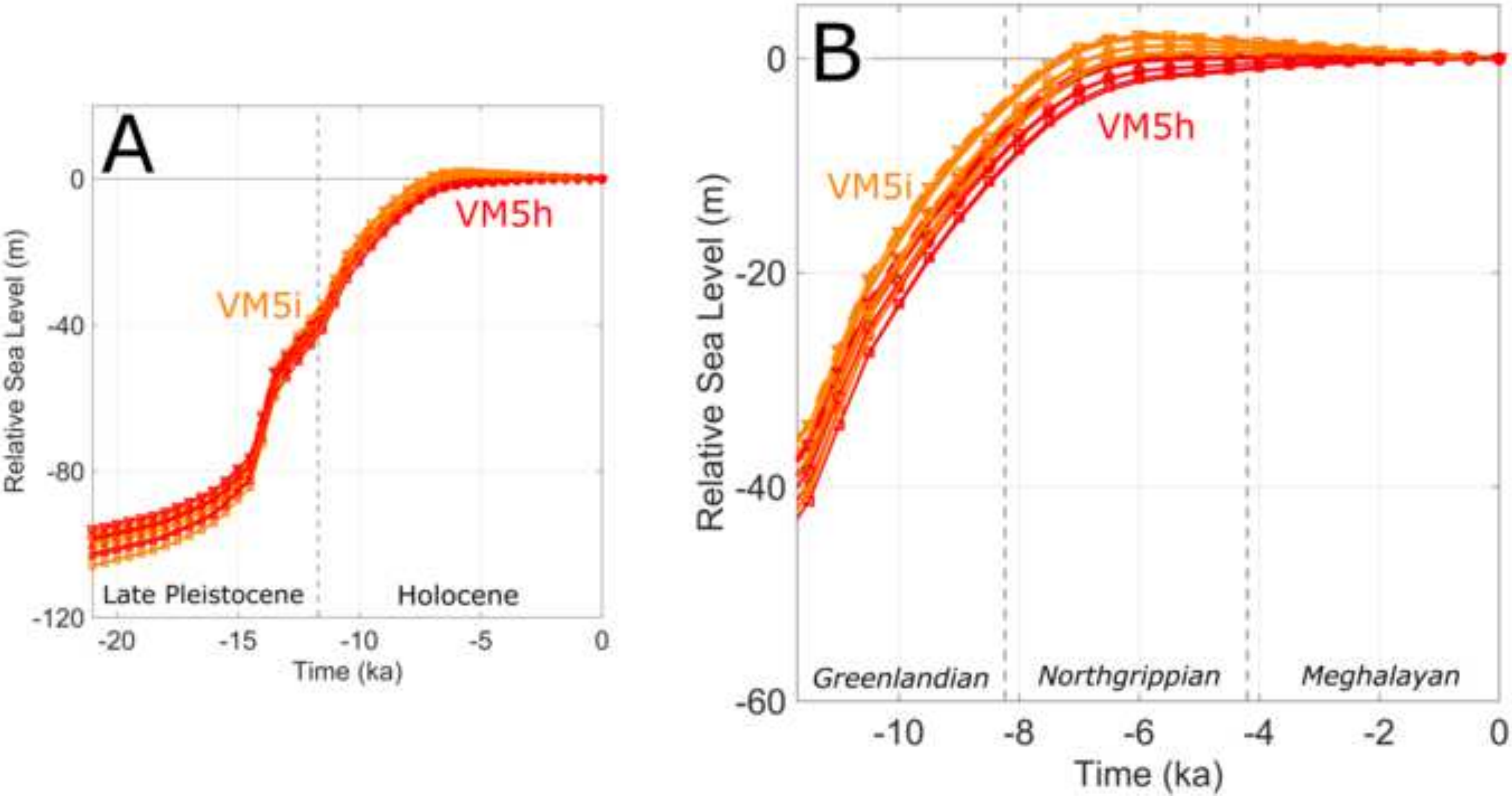
A
Relative Sea Level (m)
0
-40
-80
-120
-20
-15
-10
-5
0
Time (ka)
VM5i
VM5h
Late Pleistocene
Holocene
B
Relative Sea Level (m)
0
-20
-40
-60
-10
-8
-6
-4
-2
0
Time (ka)
VM5i
VM5h
Greenlandian
Northgrippian
Meghalayan

Fig. 7

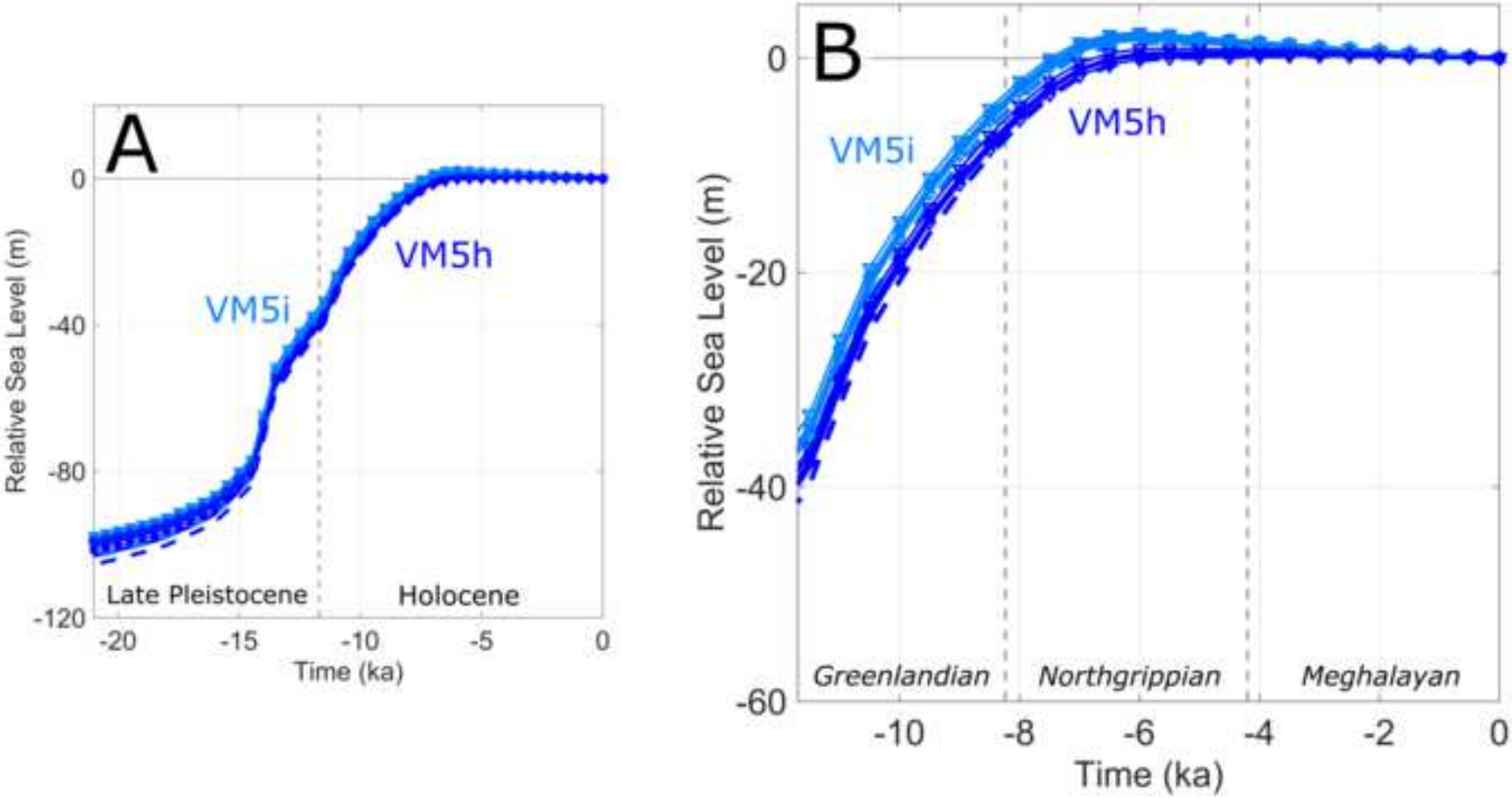
A
VM5i
VM5h
Relative Sea Level (m)
0
-40
-80
-120
-20
-15
-10
-5
0
Time (ka)
Late Pleistocene
Holocene
B
VM5i
VM5h
Relative Sea Level (m)
0
-20
-40
-60
-10
-8
-6
-4
-2
0
Time (ka)
Greenlandian
Northgrippian
Meghalayan

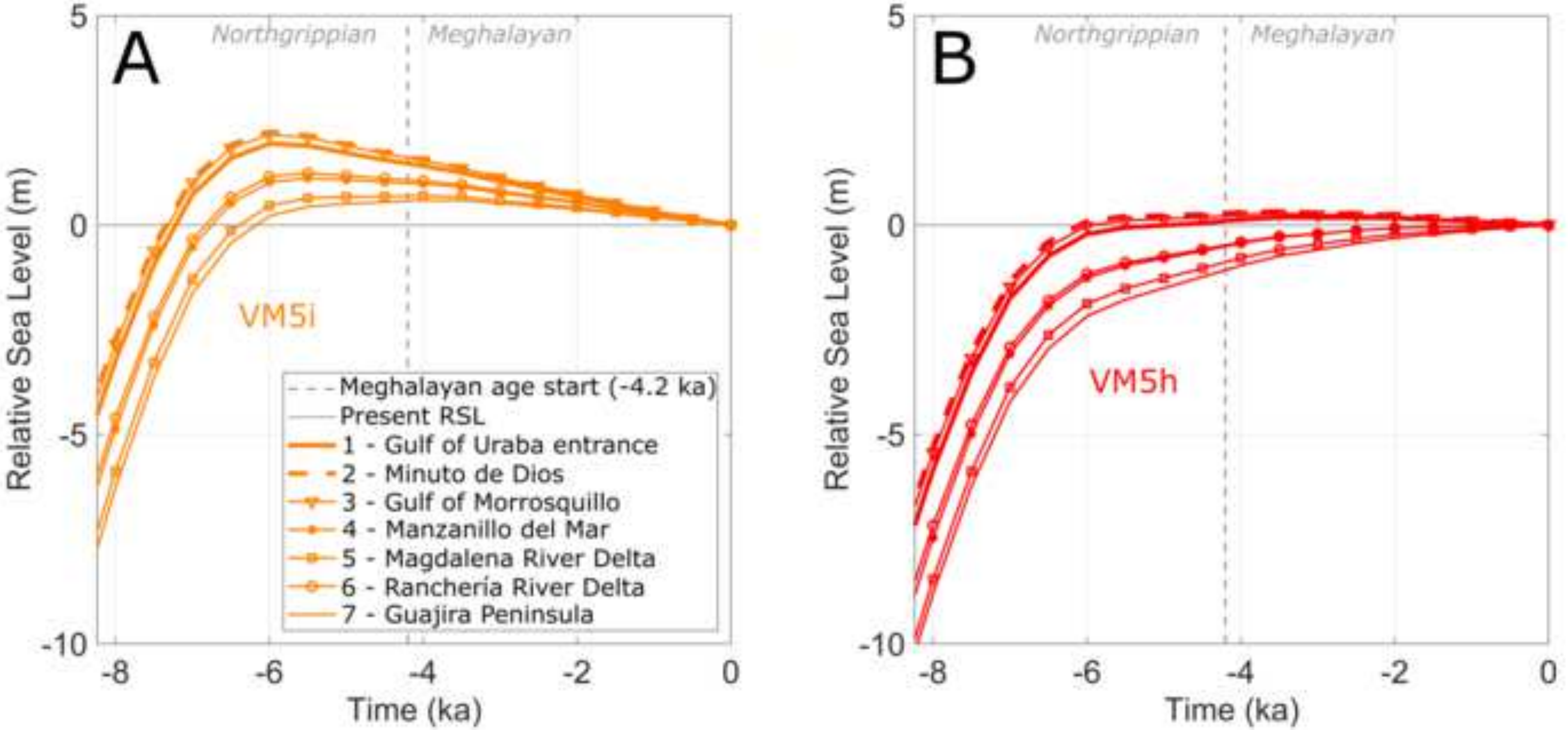
A
B
Northgrippian
Meghalayan
VM5i
VM5h
Relative Sea Level (m)
Time (ka)
5
0
-5
-10
-8
-6
-4
-2
0
Meghalayan age start (-4.2 ka)
Present RSL
1 - Gulf of Uraba entrance
2 - Minuto de Dios
3 - Gulf of Morrosquillo
4 - Manzanillo del Mar
5 - Magdalena River Delta
6 - Ranchería River Delta
7 - Guajira Peninsula

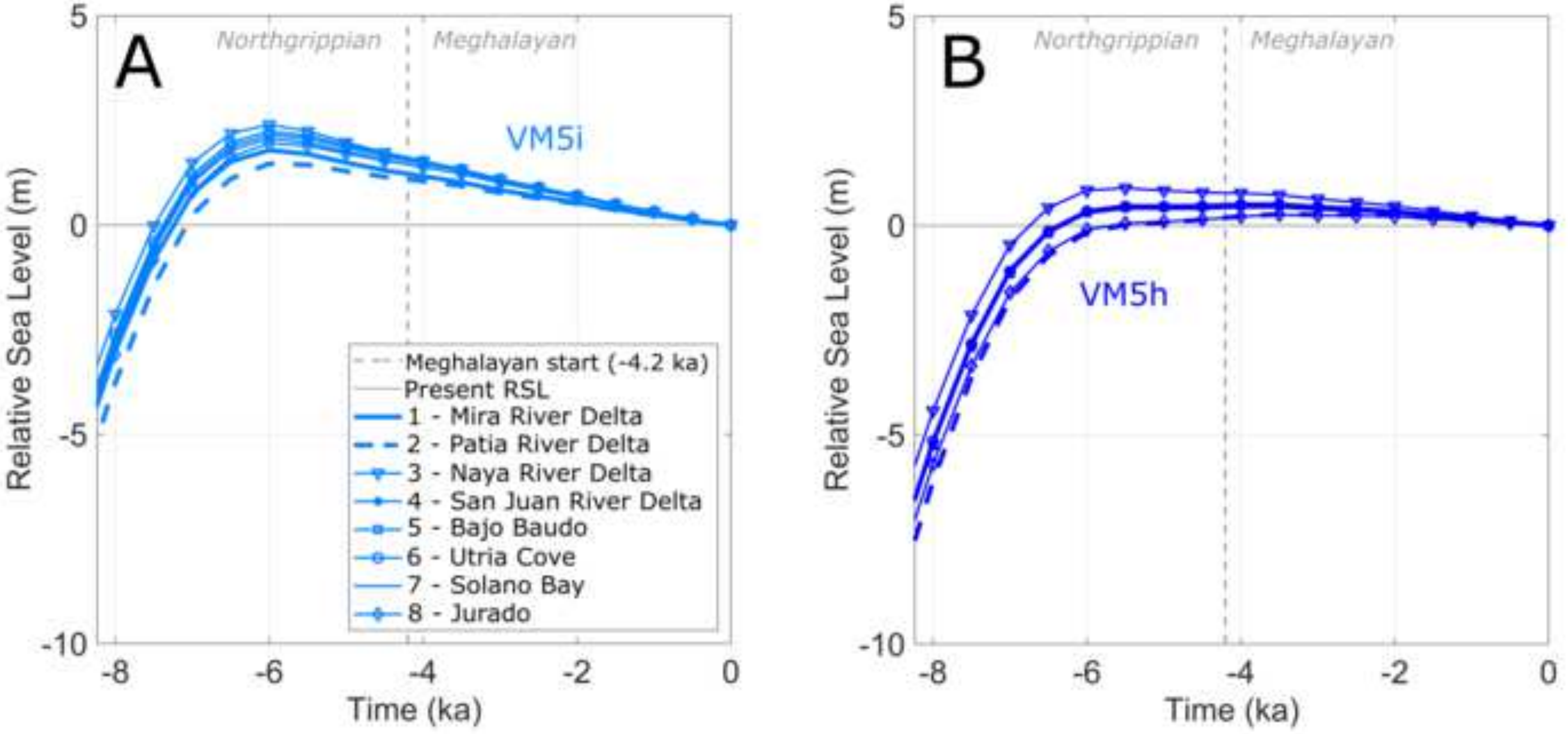
A
B
Northgrippian
Meghalayan
VM5i
VM5h
Relative Sea Level (m)
Time (ka)
5
0
-5
-10
-8
-6
-4
-2
0
Meghalayan start (-4.2 ka)
Present RSL
1 - Mira River Delta
2 - Patia River Delta
3 - Naya River Delta
4 - San Juan River Delta
5 - Bajo Baudo
6 - Utria Cove
7 - Solano Bay
8 - Jurado

Fig. 10

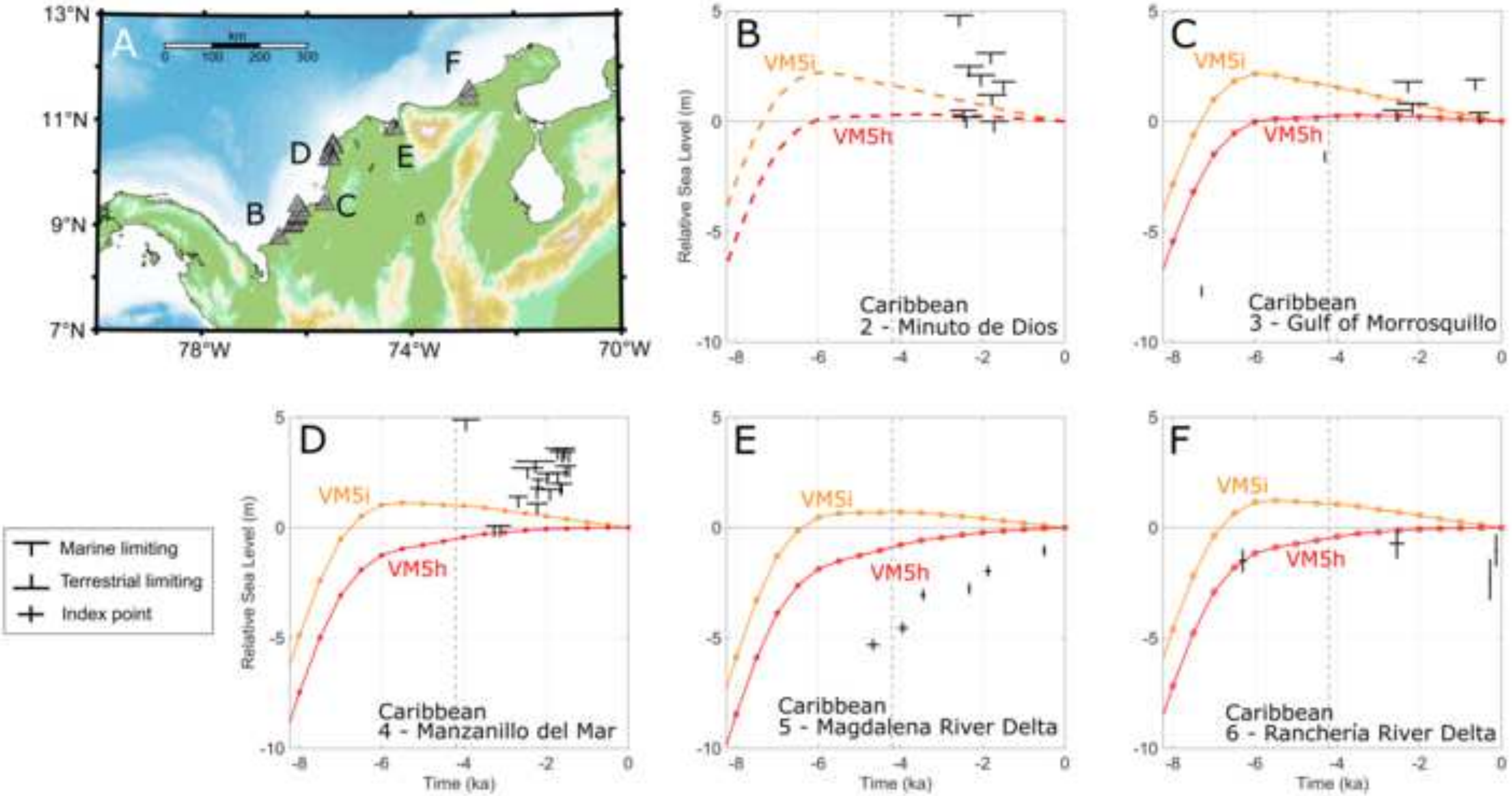
A
km
0
100
200
300
13°N
11°N
9°N
7°N
78°W
74°W
70°W
B
C
D
E
F
Relative Sea Level (m)
5
0
-5
-10
-8
-6
-4
-2
0
VM5i
VM5h
Caribbean
2 - Minuto de Dios
Caribbean
3 - Gulf of Morrosquillo
Caribbean
4 - Manzanillo del Mar
Caribbean
5 - Magdalena River Delta
Caribbean
6 - Rancheria River Delta
Time (ka)
Marine limiting
Terrestrial limiting
Index point

Fig. 11

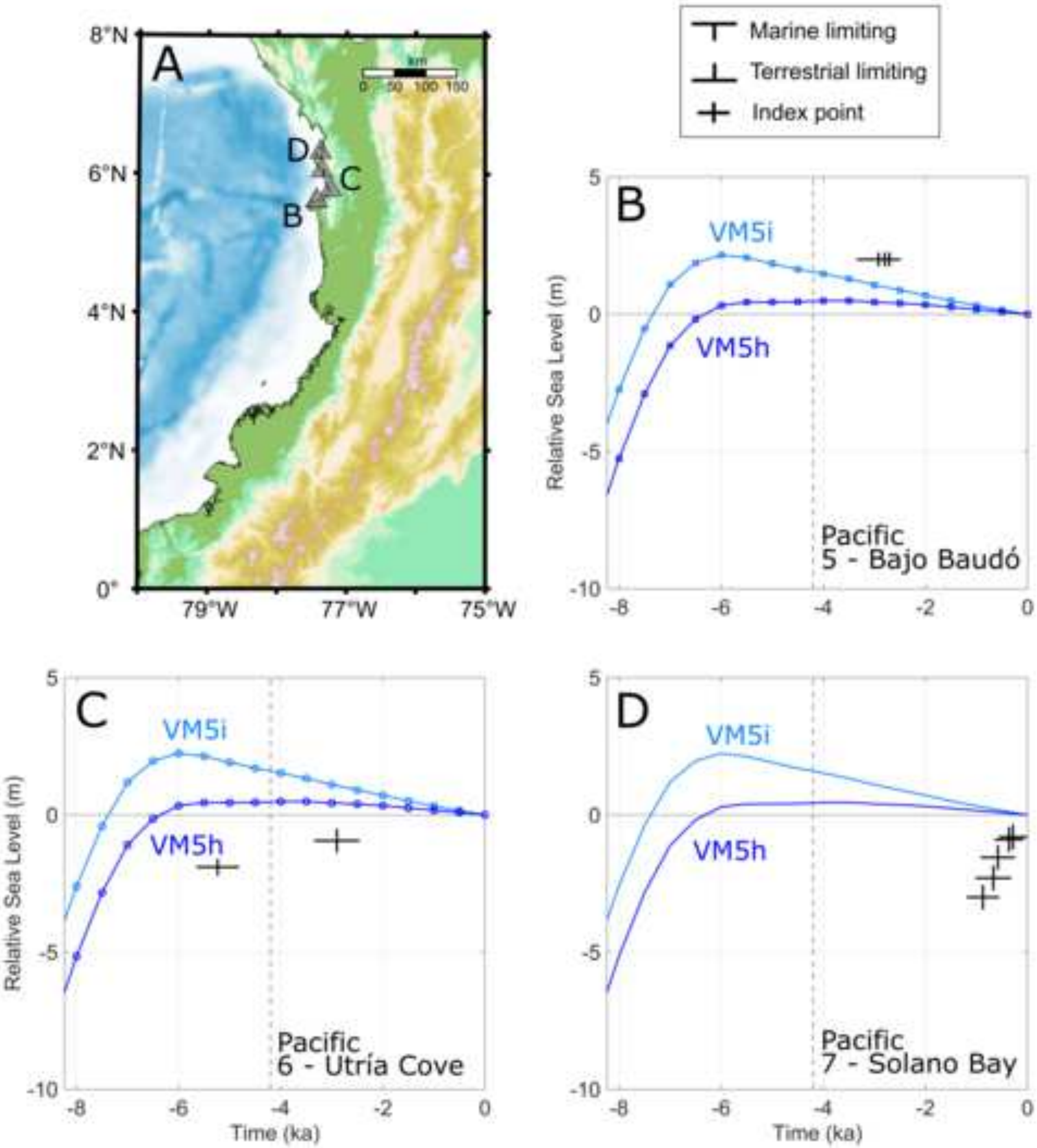
Marine limiting
Terrestrial limiting
Index point
A
8°N
6°N
4°N
2°N
0°
79°W
77°W
75°W
km
0
50
100
150
D
C
B
Relative Sea Level (m)
5
0
-5
-10
-8
-6
-4
-2
0
VM5i
VM5h
Pacific
5 - Bajo Baudó
C
VM5i
VM5h
Pacific
6 - Utría Cove
Time (ka)
D
VM5i
VM5h
Pacific
7 - Solano Bay
Time (ka)